

POLITECNICO DI TORINO

MASTER THESIS IN ELECTRICAL ENGINEERING

A.Y. 2022/2023

**Design of IPM Machines for
Traction using Rare-Earth-free
Iron-Nitride Magnets**



**Politecnico
di Torino**



Author:

Giuseppe Savio L'ABBATE

Supervisors:

Prof. Gianmario PELLEGRINO

PhD Dr. Michela DIANA

PhD Dr. Simone FERRARI

Abstract

For automotive applications, permanent magnet synchronous motors are the most common and usually contain rare-earth permanent magnets, such as neodymium magnets. The use of this type of magnet guarantees high efficiencies, torques, and power densities. However, RE elements are expensive, and there are concerns about the stability of supply and environmental damage caused by their extraction. For this reason, efforts are now being made to find an alternative to the use of rare-earth magnets, i.e. rare-earth-free magnets, in all sectors that require permanent magnets, including the automotive industry.

During this thesis work, carried out in collaboration with Volvo Cars Sweden, a synchronous motor with internal permanent magnets was designed using rare-earth-free magnets, mainly composed of iron and nitrogen, elements that are among the most abundant magnetic materials on Earth. After designing a benchmark motor with classic neodymium magnets, I moved on to design a motor that would be able to exploit rare-earth-free magnets in the best possible way, overcoming the main problems that these new materials have presented so far, namely their low resistance to demagnetization. To do this, I used the open-source software SyR-e and its function `syrmDesign`, which in the course of this work was enhanced with a function that allows demagnetization to be taken into account even during the preliminary design process.

Once the final design was defined, the geometry was optimized using JMAG software. The aim was to achieve the desired targets by minimizing the materials used and improving the behavior of the magnets against demagnetization as much as possible. Two different optimizations were carried out and finally, the results were reported for each design and a comparison was made to highlight the pros and cons of these new materials.

Acknowledgements

I would like to express my deep gratitude to my thesis supervisor Gianmario Pellegrino and my team manager Anders Thulin for allowing me to live this wonderful experience at Volvo Cars. Together with them, I would like to thank my Volvo supervisor, Michela Diana, for her continuous support throughout my work and stay in Göteborg, and Simone Ferrari for his constant help and guidance.

I want to thank Lisbeth Dahllöf and Jennifer Davis for sharing their expertise with me and Niron magnetics for the fruitful discussion and for sharing with me all the information needed to make this work possible.

I would also like to thank the entire Volvo Cars EMD team for making me feel part of the team from day one and not missing your presence and advice and making the days in the office and not so enjoyable.

I want to thank my parents who allowed me to have this experience, as well as many others. With them my brother Alessio. All together they have been a constant support over these twenty-five years. It is only thanks to you that I am here now.

I want to thank my girlfriend Gaia for these three years of support and love. For all the moments we have spent together and especially those to come. Thank you for inspiring me to look for and try experiences far from my comfort zone, for showing me how much the world and people have to offer and how much these experiences transform you inside.

I want to thank all the people commonly referred to as 'friends'. From Caltanissetta to Göteborg, through Torino. Each of you, in your own way, has been fundamental during my growth and experience. If I have not written down the names it is because I am a lucky guy and the list would be quite long.

Happiness is Only Real When Shared

Contents

Abstract	ii
1 Introduction	1
1.1 Permanent Magnet Synchronous Machines	2
1.1.1 dq axis and Equivalent Circuits	2
1.1.2 Torque	3
1.1.3 Control Strategy	4
1.2 Permanent Magnets and Demagnetization	6
1.3 Rare-Earths	8
1.3.1 Rare-Earth Elements in the Periodic Table	8
1.3.2 Rare-Earths Supply Issues	9
1.4 Possible solutions	10
2 Iron Nitrides Permanent Magnets	13
2.1 History of $\alpha'' - Fe_{16}N_2$ material	13
2.2 Iron Nitrides BH Curves Characteristics	14
3 Design of a PMSM using SyR-e	16
3.1 SyR-e Software	16
3.2 Add new Materials in SyR-e	17
3.2.1 Iron material: NO27	17
3.2.2 Magnet material: N42UH	19
3.2.3 Magnet material: Niron GEN2	20
3.3 SyR-e and Demagnetization	20
3.4 syrmDesign and FEAFix	22
4 Benchmark Motor Design	26
4.1 Number of Pins/Slots and AC losses	26
4.1.1 Types of Eddy Current Losses	26
4.1.2 Hairpin Selection	28
4.2 Initial Design Improvement	31
4.3 Selected Benchmark: L75	34

5	Design of FeN IPM motor using SyR-e	37
5.1	Reference Literature	38
5.2	1V-shape Rotor Geometry	42
5.2.1	6-pole Case	44
5.2.2	8-pole Case	45
5.2.3	12-pole Case	46
5.2.4	Summary and Conclusions	46
5.3	2V-shape Rotor Geometry	48
5.3.1	6-pole Case	48
5.3.2	8-pole Case	50
5.3.3	Summary and Conclusions	53
5.3.4	Sensitivity Analysis	54
5.4	Selected Design	56
6	Geometry Optimization using JMAG	60
6.1	GEN2 Model and Demagnetization in JMAG	61
6.2	p4-q2-mod in JMAG	63
6.3	Geometry Optimization	66
6.3.1	p4-q2-mod Optimization	67
6.3.2	Global Optimization	73
7	Final Comparisons	79
7.1	Machine Performance	80
7.1.1	Torque/Power - Speed Characteristics	80
7.1.2	Torque Ripple	80
7.1.3	Efficiency	81
7.2	Demagnetization	85
7.3	Materials and Environmental Impact	87
8	Conclusions and Future Developments	90
8.1	Conclusions	90
8.2	Future Developments	92

List of Figures

1.1	Different PMSM geometries and classification.	2
1.2	dq axes types: PM-style (a) and SR-style (b).	3
1.3	Eq. circuits for d (a) and q (b) axes in a PMSM with PM-style axis.	4
1.4	Example of MTPA and MTPV curve (a) and current control (b)	5
1.5	Normal curve $B(H)$ and intrinsic curve $J(H)$	6
1.6	Magnet operating trajectory during demagnetization.	8
1.7	Periodic Table of the Elements with rare-earth elements (REEs) highlighted.	9
1.8	Global Rare-Earth Reserves by Country in 2017, source [3].	10
1.9	Global Rare-Earths Production by Country in 2019, source [4].	11
3.1	Data flow used by SyR-e [14].	16
3.2	SyR-e main GUI.	17
3.3	SyR-e MMM GUI.	18
3.4	Datasheet iron loss (red circles) and interpolating surface (10).	19
3.5	NO27 data in SyR-e.	20
3.6	N42UH data in SyR-e.	21
3.7	Example of a syrmDesign plane.	23
3.8	SyR-e geometric parameters [16].	24
3.9	syrmDesign Explorer GUI.	24
4.1	Different types of eddy current losses [17].	27
4.2	Benchmark cross-section.	28
4.3	Torque limits: 6-pin vs 8-pin.	29
4.4	Stator Joule losses: 6-pin vs 8-pin.	30
4.5	Efficiency map: 6-pin vs 8-pin.	31
4.6	Torque limits: L95 vs L75.	32
4.7	Efficiency map: L95 vs L75.	33
4.8	Demagnetization current and HWC three-phase short-circuit current.	35
5.1	Paper reference geometry [19].	39
5.2	Geometry parameters in the V-shape case.	41
5.3	p3-q2 1V: A_{diff} vs current density.	43
5.4	p4-q2 1V: A_{diff} vs current density.	43
5.5	p6-q2 1V: A_{diff} vs current density.	43

5.6	p3-q2 1V 20 A/mm ² : <i>xb</i> plane design (on the left) and Demagnetization Analysis result (on the right).	44
5.7	p3-q2 1V 15 A/mm ² <i>xb</i> plane: Torque and A_{diff} .	45
5.8	p4-q2 1V 10 A/mm ² : <i>xb</i> plane design (on the left) and Demagnetization Analysis result (on the right).	46
5.9	p6-q2 1V 10 A/mm ² : <i>xb</i> plane design (on the left) and Demagnetization Analysis result (on the right).	47
5.10	p3-q2 2V: A_{diff} vs current density.	49
5.11	p4-q2 2V: A_{diff} vs current density.	49
5.12	p6-q2 2V: A_{diff} vs current density.	49
5.13	p3-q2 2V 20 A/mm ² : <i>xb</i> plane design (on the left) and Demagnetization Analysis result (on the right).	50
5.14	p3-q2 2V 15 A/mm ² <i>xb</i> plane: Torque and A_{diff} .	50
5.15	p4-q2 2V 20 A/mm ² <i>xb</i> plane: Torque and A_{diff} .	51
5.16	p4-q2 2V 15 A/mm ² : <i>xb</i> plane design (on the left) and Demagnetization Analysis result (on the right).	52
5.17	p4-q2 2V 10 A/mm ² <i>xb</i> plane: Torque and A_{diff} .	52
5.18	p4-q2 2V 15 A/mm ² after sensitivity analysis: <i>xb</i> plane design (on the left) and Demagnetization Analysis result (on the right).	54
5.19	Tooth size factor sensitivity analysis.	55
5.20	Stator yoke factor sensitivity analysis.	55
5.21	Rotor yoke factor sensitivity analysis.	55
5.22	Characteristics of the p4-q2-mod motor.	57
5.23	Cross section geometry: from p4-q2-ideal to p4-q2-mod.	57
6.1	JMAG logo.	60
6.2	JMAG non-linear magnet model (<i>Point Array</i>).	61
6.3	p4-q2-mod cross section in JMAG.	64
6.4	Characteristics of the p4-q2-mod motor on JMAG.	65
6.5	p4-q2-mod JMAG Demagnetization Ratio contour plot.	65
6.6	p4-q2-mod optimization parameters.	69
6.7	Optimization results: Torque-A1%.	69
6.8	Optimization results: Torque-A1% best cases.	70
6.9	Optimization results: Torque-A5%.	70
6.10	Optimization results: Torque-A5% best cases.	71

6.11	SyR-e optimization: chosen design.	72
6.12	Characteristics of the 1713 motor.	72
6.13	Global optimization parameters.	73
6.14	Optimization results: Torque-A1%.	74
6.15	Optimization results: Torque-A1% best cases.	74
6.16	Optimization results: Torque-A1%.	75
6.17	Optimization results: Torque-A5% best cases.	75
6.18	Global Optimization: chosen design.	76
6.19	Characteristics of the 7823 motor.	77
7.1	Comparison of the cross-section geometry of the designs.	79
7.2	Comparison of torque and power limit curves.	81
7.3	Comparison of torque ripple.	82
7.4	Comparison of efficiency maps.	83
7.5	Comparison of SyR-e design efficiency maps calculated with the two software.	84
7.6	Comparison of A1% values on full torque-speed maps.	86

List of Tables

3.1	Steinmetz coefficients used.	18
4.1	Design targets.	26
4.2	Comparison of 6-pin and 8-pin motors.	29
4.3	Joule losses comparison @ 120 km/h	30
4.4	Efficiency points: 6-pin vs 8-pin.	31
4.5	Materials: 6-pin vs 8-pin.	32
4.6	Efficiency points: L95 vs L75.	33
4.7	Materials: L95 vs L75.	33
4.8	L75 summery data.	34
5.1	1V-shape best designs.	47
5.2	2V-shape best designs.	53
5.3	p4-q2 motors recap.	58
6.1	Optimization objective functions.	68
6.2	Optimization results best cases.	71
6.3	Global optimization results best cases.	76
7.1	Final comparison.	80
7.2	Efficiency points comparison.	84
7.3	Materials and environmental impact data comparison.	88

List of Acronyms

EV	Electric Vehicle
HEV	Hybrid Electric Vehicle
PM	Permanent Magnet
PMSM	Permanent Magnet Synchronous Motor
SPM	Surface Permanent Magnet
IPM	Internal Permanent Magnet
RE	Rare Earth
REE	Rare Earth Element
SynRM	Synchronous Reluctance Motor
PMASynRM	Permanent magnet-assisted Synchronous Reluctance Motor
HVAC	Heating, ventilation, and air conditioning
SR	Synchronous Reluctance
MTPA	Maximum Torque Per Ampere
EMF	Electromotive Force
MTPV	Maximum Torque Per Volt
LREE	Light Rare Earth Elements
HREE	Heavy Rare Earth Elements
FeN	Iron Nitride
FEA	Finite Element Analysis
MOOA	Multi-Objective Optimization Algorithms
GUI	Graphical User Interfaces
MMM	Magnetic Model Manipulation
HWC	Hyper Worst Case
ASC	Active Short-Circuit

FASR	Ferrite-Assisted Synchronous Reluctance
MODE	Multi-Objective Differential Evolution
MOGA	Multi-Objective Genetic Algorithm
EPS	Environmental Priority Strategies
ELU	Environmental Load Units
UGO	Uncontrolled Generator Operation
VFM	Variable Flux Machine

1 Introduction

The requirements of electric motors for automotive applications such as electric vehicles (EVs) and hybrid electric vehicles (HEVs) include high torque density, high power density, a wide speed range, and high efficiency. In such applications, permanent-magnet (PM) synchronous motors (PMSMs) are the most popular. PMSMs can be classified according to the position of the magnets in the rotor into Surface-mounted Permanent Magnet (SPM) and Internal Permanent Magnet (IPM) machines. The former have the magnets on the outer surface of the rotor, giving rise to isotropic motors, while the latter has the magnets buried inside the rotor core, resulting in motors characterized by a certain anisotropy, depending on the shape and position of the barriers in which the magnets are located.

PMSMs usually contain rare-earth (RE) PMs: such as neodymium magnets (NdFeB). PMSMs with RE PMs have high efficiencies, high power factors, high torque, and power density. However, RE PMs are high in cost, and there is concern about the stable supply of RE materials and the environmental damage caused by their mining. Therefore, electric motors with less or no RE PMs are required in EV and HEV applications.

The Synchronous Reluctance Motor (SynRM) does not use PMs, and thus, it is one solution for achieving a RE-free motor. On the other hand, it is inferior in torque density, power factor, and efficiency compared to PMSMs. By adding the proper amount of the PM to SynRM, the torque density and power factor can be improved; this is called a PM-assisted SynRM (PMASynRM) [1]. Fig. 1.1 shows examples of the different PMSM geometries described with their classification.

Therefore, finding a viable alternative to RE magnets would be very important, given the ever-increasing demand for them. Indeed, RE PMs are used not only in the automotive sector, but also in common everyday devices such as computers, household appliances, audio speakers, HVAC (heating, ventilation, and air conditioning), and other devices that are crucial for the transition to green energy, such as wind turbines.

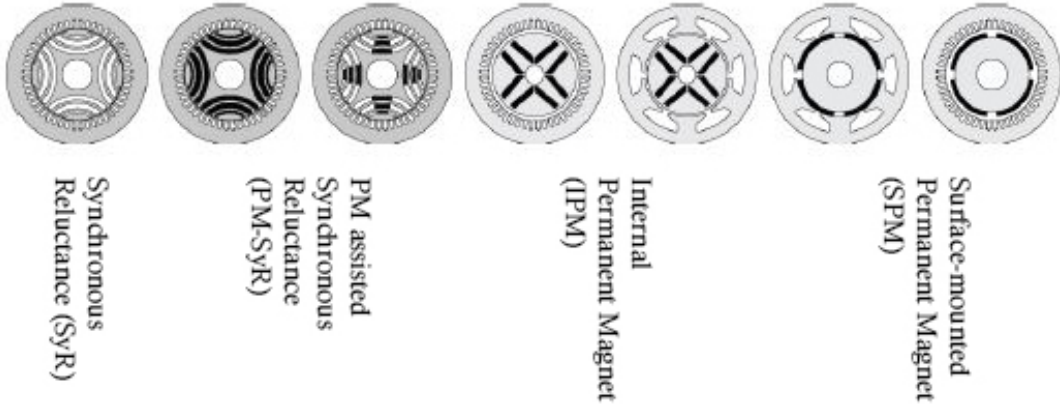


Figure 1.1: Different PMSM geometries and classification.

1.1 Permanent Magnet Synchronous Machines

1.1.1 dq axis and Equivalent Circuits

The PMSM is mainly studied in the dq axes system. The advantage of the dq axes system is that it is a stationary axes system with respect to the rotating vectors. Depending on the type of PMSM, the definition of the reference axis system may change. When the d-axis is aligned with the flux produced by the magnets, the axis system is called PM-type (Permanent Magnet) while a SR-type (Synchronous Reluctance) axis system is defined with the d-axis aligned to the maximum permeance direction. It follows that the flux of the magnets (when present) will be aligned in the -q direction.

The PM-type system will be used from now on.

Physical quantities in the abc system such as current, voltage, flux linkage, etc. can be transformed in the dq system. A transformation matrix that allows this conversion is:

$$[T]_{dq0,abc} = \frac{2}{3} \begin{bmatrix} \cos(p\theta_r) & \cos(p\theta_r - \frac{2\pi}{3}) & \cos(p\theta_r + \frac{2\pi}{3}) \\ -\sin(p\theta_r) & -\sin(p\theta_r - \frac{2\pi}{3}) & -\sin(p\theta_r + \frac{2\pi}{3}) \\ 1/2 & 1/2 & 1/2 \end{bmatrix} \quad (1)$$

where θ_r is the rotor angle and p is the number of pole pairs.

The voltage equation of the machine in abc system is:

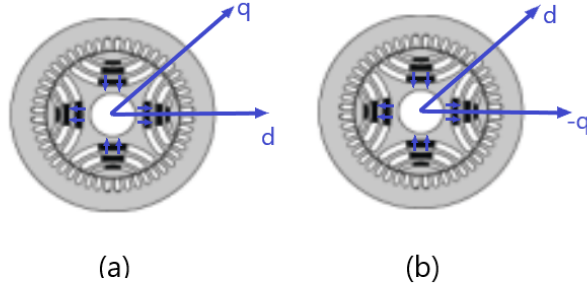


Figure 1.2: dq axes types: PM-style (a) and SR-style (b).

$$\bar{v}_{abc} = R_s \bar{i}_{abc} + \frac{d\bar{\lambda}_{abc}}{dt} = R_s \bar{i}_{abc} + \frac{d}{dt} (\bar{\lambda}_{PM,abc} + [L]_{abc} \bar{i}_{abc}) \quad (2)$$

where $\bar{v}_{abc} = [v_{a,n} \ v_{b,n} \ v_{c,n}]^T$ is the vector with the phase voltages, R_s is the stator resistance, $\bar{\lambda}_{PM,abc}$ is the permanent magnet flux linkage, $[L]_{abc}$ is the inductance matrix.

After converting (2) from abc to dq system it can be expressed as:

$$\begin{cases} v_d = R_s i_d + \frac{d\lambda_d}{dt} - \omega \lambda_q \\ v_q = R_s i_q + \frac{d\lambda_q}{dt} + \omega \lambda_d \end{cases} \quad (3)$$

where $\lambda_d = \lambda_{PM} + L_d i_d$, $\lambda_q = L_q i_q$, λ_{PM} is the peak PM flux linkage and ω is the electrical speed equal to pole pairs times mechanical rotor speed, $\omega = p\omega_r$.

The equivalent circuits referring to equations (3) are shown in Fig. 1.3.

1.1.2 Torque

For a general formulation, the torque produced by a PMSM is the combination of two contributions: PM torque and reluctance torque. The torque equation is written as in (4). In the SPM case, the reluctance contribution is zero, and vice versa in the SyR case, the magnets' contribution is zero.

$$T_e = T_{e,PM} + T_{e,rel} = \frac{2}{3} p [\lambda_{PM} i_q + (L_d - L_q) i_d i_q] \quad (4)$$

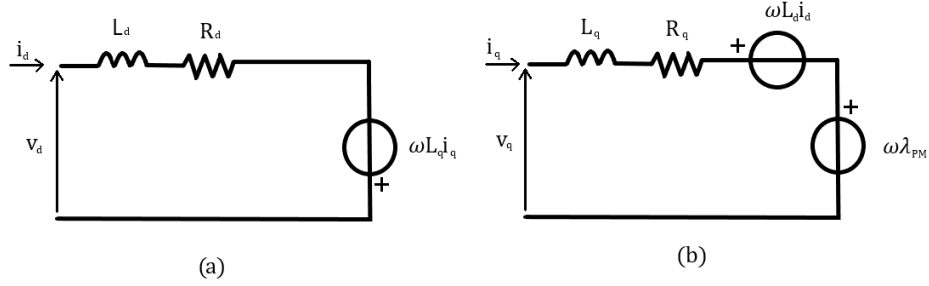


Figure 1.3: Eq. circuits for d (a) and q (b) axes in a PMSM with PM-style axis.

The PM torque is produced by the q-axis current and magnet flux while the reluctance torque contribution comes from the difference in the d and q axes inductance. When the PM-style axes are used the magnetic inductance along the d axis is very low (high reluctance) and $L_d < L_q$ so to have a positive contribution from the reluctance torque it is necessary to have $i_d < 0$.

1.1.3 Control Strategy

The motor is supplied with a three-phase voltage from the inverter. The voltage and current limitation from the inverter can be expressed as:

$$\sqrt{v_d^2 + v_q^2} \leq V_{max} = \frac{v_{dc}}{\sqrt{3}} \quad (5)$$

$$\sqrt{i_d^2 + i_q^2} \leq I_{max} \quad (6)$$

where v_{dc} is the maximum dc-link voltage, $\frac{v_{dc}}{\sqrt{3}}$ is the maximum peak phase voltage, and I_{max} is the maximum current from inverter.

Usually, the best way to supply the motor from zero speed to base speed is along the Maximum Torque Per Ampere (MTPA) curve. This characteristic minimize conduction losses and then defines the optimum current angle to maximize torque. By writing the supply current as a function of current magnitude $|\bar{I}|$ and angle γ (defined from the q-axis) (7) it is possible to describe how the torque changes as the angle of the current vary (8).

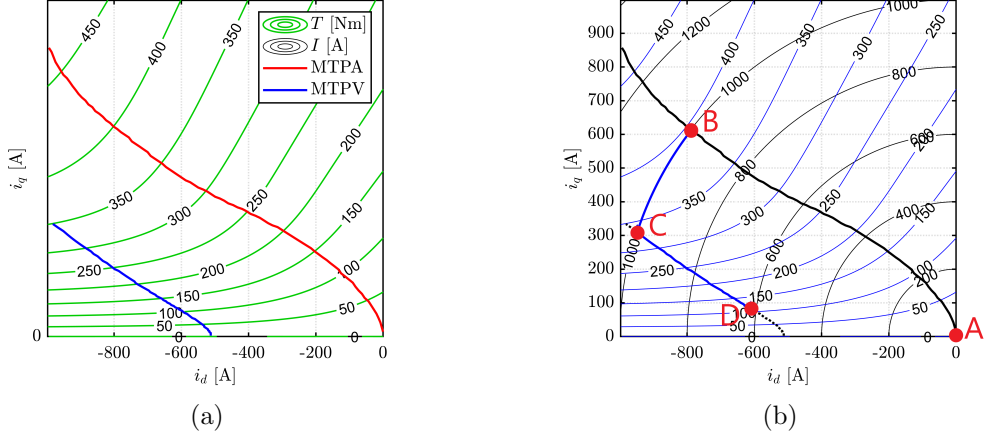


Figure 1.4: Example of MTPA and MTPV curve (a) and current control (b)

$$\begin{cases} i_d = |\bar{I}| \cos(\gamma) \\ i_q = -|\bar{I}| \sin(\gamma) \end{cases} \quad (7)$$

$$T_e = \frac{2}{3} p |\bar{I}| [\lambda_{PM} \cos(\gamma) - (L_d - L_q) |\bar{I}| \cos(\gamma) \sin(\gamma)] \quad (8)$$

The value of γ angle for which $\frac{dT_e}{d\gamma} = 0$ is defined as γ_{MTPA} and produces the MTPA curve, which as can be seen in Fig.1.4 (a) is non-linear, due to non-linear iron saturation.

In order to increase the speed beyond the base speed (operating point at which the inverter reach its voltage limit V_{max}), the current vector is rotated anticlockwise, thus moving the current from the q-axis to the d-axis (see Fig. 1.4(b) from point B to point C). The current component along the d-axis counteracts the increase in the back electromotive force (EMF) as described from the q-axis equivalent circuit in Fig.1.3 (b). Another curve of interest is the Maximum Torque Per Volt (MTPV). If rotating the current MTPV is intercepted, the magnitude of the current will be decreased to move the current vector along this curve up to the maximum speed value (Fig. 1.4(b) from point C to point D).

1.2 Permanent Magnets and Demagnetization

PM materials have two distinct characteristics: one is that they can be strongly magnetized under the action of external magnetic field, the other one is hysteresis, they still remain magnetized after removing the external magnetic field. The relationship between the change of external magnetic field and the change of permanent magnet magnetism can be described by two curves, namely normal curve (B-H curve) and intrinsic curve (J-H curve), that can be seen in Fig.1.5. The normal curve represents the magnetic field contributed by both the applied field and the magnet, while the intrinsic curve represents only the magnetic field of the magnet. The relationship between these quantities is:

$$B = \mu H = \mu_0(H + M) = \mu_0 H + J \quad (9)$$

where $\mu_0 = 4\pi \cdot 10^{-7} \text{ H/m}$ is the vacuum permeability.

Both normal and intrinsic curves are widely used in PMs analysis. Characteristic points of these curves include: B_r , called *remanence*, is the magnetization left in a ferromagnetic material, H_{cB} , called *coercivity*, is the value of H for which B is zero and H_{cJ} , called *intrinsic coercivity*, is the value of H for which J is zero.

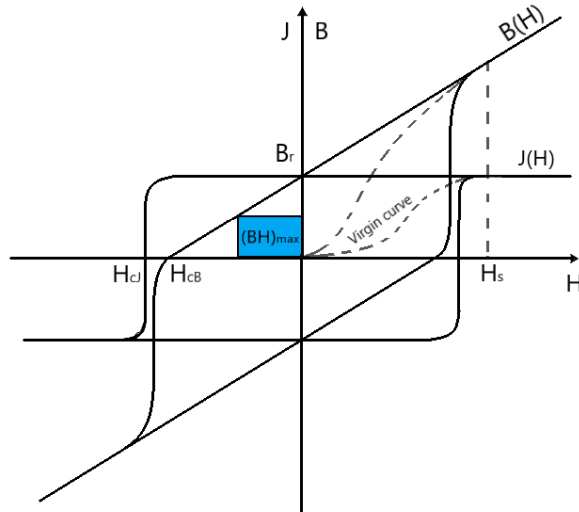


Figure 1.5: Normal curve $B(H)$ and intrinsic curve $J(H)$.

For PMs, the second quadrant of the characteristics is the most relevant one. A

key figure of merit of PMs is the *Maximum Energy Product* $(BH)_{max}$. It is defined as the maximum value of $(-BH)$ along the B-H curve and it can be graphically defined as the area of the largest rectangle that can be drawn between the origin and the normal curve (Fig.1.5). $(BH)_{max}$ is typically given in units of either kJ/m^3 (kilojoules per cubic meter, in SI electromagnetism) or $MGOe$ (mega-gauss-oersted, in gaussian electromagnetism). $1 MGOe$ is equivalent to $7.958 kJ/m^3$.

The normal curve has a point delimiting the linear behavior of the magnet in the second quadrant. At this point, called *knee point*, the normal curve slope begins to change dramatically. With reference to Fig. 1.6, if the magnet is pushed to work at point P2 and the external field is removed, the magnet operating point will reverse back along the trajectory indicated by the red arrow, called *recoil line* to a lower magnetic remanence value B_{r2} . This causes an irreversible loss of flux density of the magnet, which is then considered *irreversibly demagnetized*. This does not happen if the working point is located before the knee point, for example point P1, in the *linear* (or *reversible*) region. It is interesting to note that the slope of the linear region determines the slope of all recoil lines, which are all parallel to the linear section.

When a piece of magnet is placed in a uniform demagnetizing field that covers the entire magnet, all points of the magnet operate under the same condition, assuming that the material's magnetic properties are uniform. If the magnet is demagnetized under such a uniform demagnetizing field, this is called global demagnetization. The normal curve can be directly used to analyze the effects of global demagnetization because the magnetic condition of the magnet can be represented by one single operating point on the curve.

However, when the demagnetization field is not uniform, only covers some portions of the magnet or has spatially varying magnetic properties, different regions of the magnet will operate under different operating conditions. Local demagnetization is used to describe the case where some portions of the magnet are demagnetized while the others are not. During operation, the magnets in a PMSM are more vulnerable to local demagnetization and it is of course more challenging to analyze [2].

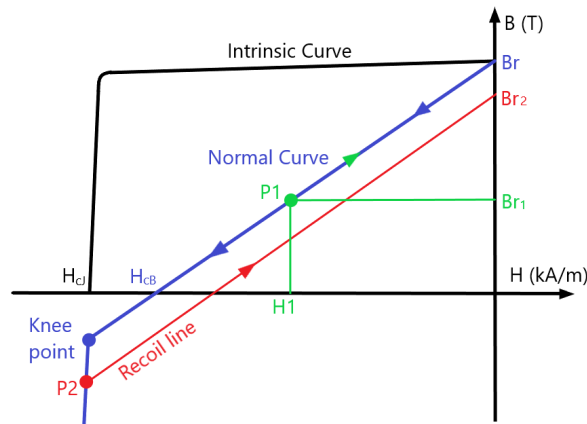


Figure 1.6: Magnet operating trajectory during demagnetization.

1.3 Rare-Earths

1.3.1 Rare-Earth Elements in the Periodic Table

The Rare-Earth Elements (REEs), also called lanthanides (though yttrium and scandium are usually included as rare-earths) are a set of 17 nearly-indistinguishable lustrous silvery-white metals. Scandium and yttrium are considered rare-earth elements because they tend to occur in the same ore deposits as the lanthanides and exhibit similar chemical properties but have different electronic and magnetic properties.

The RE metals are grouped into Light Rare-Earth Elements (LREE) and Heavy Rare-Earth Elements (HREE). The LREE category consists of elements from lanthanum to samarium while the HREE category includes elements from europium to lutetium plus yttrium. The classification is determined by the electron configuration of the atoms of the element. Scandium forms a trivalent cation, like the other REEs, but it does not meet the electron configuration criterion for an LREE and does not share enough chemical properties with the HREE to be considered one of them.

Despite the name, these elements are fairly abundant in the Earth's crust. The most abundant REE is cerium, which is actually the 25th most abundant element in Earth's crust (approximately as common as copper).

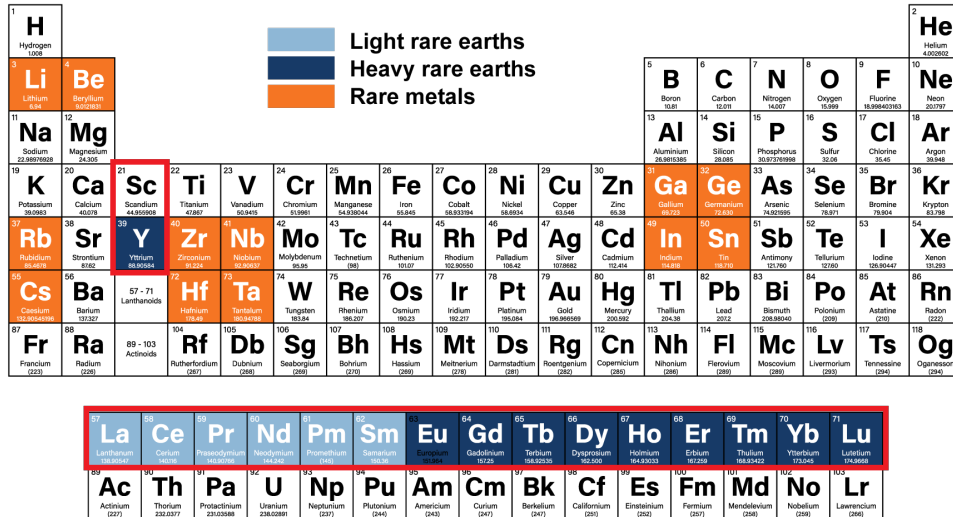


Figure 1.7: Periodic Table of the Elements with rare-earth elements (REEs) highlighted.

1.3.2 Rare-Earths Supply Issues

Although REEs are relatively abundant in the Earth’s crust, their extractable concentrations are less common than for most other mineral raw materials. Consequently, economically exploitable ore deposits are sparse (i.e. ”rare”), making the cost of rare-earths very high. But it is not just about the financial cost.

REs mining carries a huge environmental price to pay. Indeed, once the ore containing the rare-earths has been dug up, it will often end up in a big leaching pool, where chemicals are used to separate them out from all the other elements. But these pools can release dangerous chemicals into the air and if they are badly sealed, chemicals can also seep into the ground, getting into groundwater.

Another relevant fact is that few countries are involved in REs production. China controls by far the biggest share of the world’s REs reserves but there is also a high concentration of them in Vietnam, Brazil and Russia (Fig.1.8).

However, when it comes to actually refining and processing, China is even

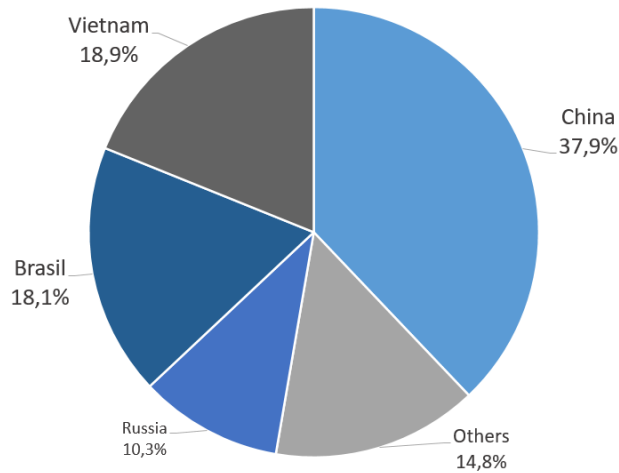


Figure 1.8: Global Rare-Earth Reserves by Country in 2017, source [3].

further ahead (Fig.1.9).

This represents a risk if one of the countries will stop exporting the material. According to [5] In 2010, China’s decision to reduce its export quota of REEs by 40 percent raised serious concerns among its major customers: European Union, Japan and the United States.

1.4 Possible solutions

NdFeB magnets are widely used for conversion between electricity and mechanical energy and beyond. Neodymium (Nd) is part of the RE family but is not the only one present. It is also important to recognise that a key ingredient in allowing NdFeB magnets to operate at high ambient temperatures is Dysprosium (Dy). In fact magnetic properties of NdFeB, without Dy, is strongly temperature dependent.

A large share of the magnet market is occupied by hard ferrites because of their low cost, their excellent thermal stability, and because their properties are good enough for most motors that do not have power density requirements [6]. In fact, two of the main problems with ferrites are limited magnetic force, with much lower flux density values than RE PMs, and poor resistance to demagnetization. Therefore, for motors that have stringent weight and size limitations, such as the traction motor of electric vehicles, other solutions are required.

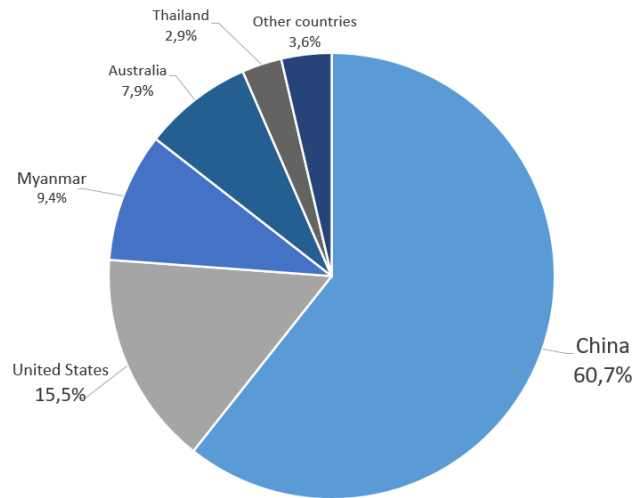


Figure 1.9: Global Rare-Earths Production by Country in 2019, source [4].

One possible solution might be to try to create a circular economy where neodymium magnets are recycled, reprocessed, and reused. That is why the European Union started a project in 2019 that will end in 2023 [7]. The aim of this project (called SUSMAGPRO) is to identify, separate, recycle, and demonstrate recycled magnets at a pilot scale with a multidisciplinary team located across the European Union. The project targets three of the main application sectors including automotive, electronics, and wind turbines.

However, a definite solution would be to find a viable alternative to magnets that contain REEs, namely RE-free magnets. In the past years, great progress has been made toward improving the microstructure and physical properties of RE-free PMs. Several new candidate materials systems were investigated, and some have shown realistic potential for replacing RE PMs in some applications.

2 Iron Nitrides Permanent Magnets

Among RE-free PMs materials, iron nitrides (FeN) attract considerable interest due to their exceptionally high magnetization and because their elements are the most abundant of all magnetic materials on Earth. Iron nitrides can also offer versatile magnetic properties originating from various crystal structures with different nitrogen concentrations in the lattice. Among them, metastable $\alpha'' - Fe_{16}N_2$ is considered one of the most promising as a candidate for RE-free magnets.

2.1 History of $\alpha'' - Fe_{16}N_2$ material

The discovery of the magnetic properties of this type of material, and of the $\alpha'' - Fe_{16}N_2$ structure in particular, is not new. K.H. Jack first found the existence of the $\alpha'' - Fe_{16}N_2$ phase in 1951 [8]. He reported this iron nitride phase as a metastable phase that was formed from a rapid quenching process from γ -Fe-N-austenite. At that time, not much attention was given to the magnetic properties of this material.

In 1972, Kim and Takahashi claimed a giant saturation magnetization as high as 2.58 T on the FeN thin films with partial $\alpha'' - Fe_{16}N_2$ phase [9]. Twenty years later, many magnetic researchers tried to repeat their results because of the emerging demand for high-saturation magnetization materials. In the 1990s, Sugita's group at Hitachi Central Lab reported that single crystal $\alpha'' - Fe_{16}N_2$ films could possess a saturation magnetization as high as 3.23 T at low-temperature [10]. This unique iron nitride phase immediately attracted attention from the magnetic community, inspiring many groups around the world to explore this material using different preparation methods. However, the poor reproducibility of this phase's giant saturation magnetization led to a decline in research on this topic and was a mystery in magnetic materials and magnetism.

In the last 10 years, the topic has attracted much more attention in the magnetic community because of its RE-free, high saturation magnetization, and high anisotropic energy [11].

2.2 Iron Nitrides BH Curves Characteristics

Niron Magnetics, born in 2012 in the University of Minnesota laboratory, is developing FeN RE-free magnets. Using a patented process, Niron aims to produce high-powered magnets using commonly available iron and nitrogen raw materials that can be sourced globally and sustainably.

For the purpose of this work, to advance the development of next-generation motors in parallel with the development of next-generation materials, Niron provided proprietary protected BH curves that were the basis of this analysis. The second generation of Niron magnets, called GEN2, was used for the work in this thesis.

The critical elements of the BH curves describing these magnets are:

- high remanence values, with values greater than remanence of some commercially available NdFeB magnets;
- low temperature coefficients, which allows stable performance throughout the motor operating temperature range and more favorable relative performance than NdFeB at high operating temperatures;
- lower coercivity compared with commercially available NdFeB grades with values more similar to those of hard ferrites and the presence of a knee in the second quadrant, which must be taken into account to avoid incurring demagnetization during operation.

Niron's understanding of next-generation FeN-based PMs is based upon empirical measurements of current FeN powder, coupled with targets for the microstructure that can be achieved when forming that powder into a bulk magnet and specific process improvements on the development roadmap.

3 Design of a PMSM using SyR-e

3.1 SyR-e Software

SyR-e (Synchronous Reluctance - evolution) [12] is an open-source software, developed in Matlab/Octave, born from the collaboration between Politecnico di Torino and Politecnico di Bari in 2009 and available online since 2014. SyR-e was created to design SynRM by means of finite element analysis (FEA) and multi-objective optimization algorithms (MOOA). After a considerable amount of upgrades, SyR-e has been enriched with new functionalities, including PMASynRM, SPM, and IPM machine design. The introduction of the initial design procedure (`syrmDesign`) has also been a key contribution, which allows a preliminary design in a short time. The finite element analysis is performed with the free software FEMM [13], a finite element solver for 2D magnetic problems. A Matlab script creates a parameterized drawing of a synchronous machine as a `.fem` file that is quickly analyzed by the FEA software. The continuous rotation of the rotor is emulated in FEMM by running several simulations at different rotor positions. The principle of operation of SyR-e is represented in Fig. 3.1. GNU Octave can replace Matlab for all mentioned purposes.

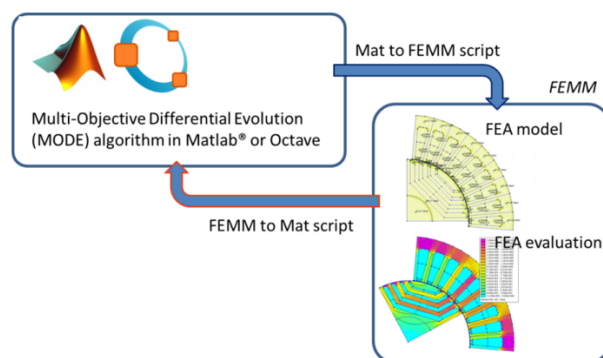


Figure 3.1: Data flow used by SyR-e [14].

SyR-e can be used in Matlab through two Graphical User Interfaces (GUIs), one for the design and FEA analysis (main GUI) in Fig. 3.2 and the other for magnetic model manipulation (identified with the acronym MMM) in Fig. 3.3. The main GUI allows you to set the design data, specify the geometrical parameters of the

stator and rotor, define the type of winding of the machine, and select the materials used. Above all, it allows various magnetic simulations to be carried out, such as evaluating torque and power factor at a single operating point, evaluating flux maps and iron losses, and more.

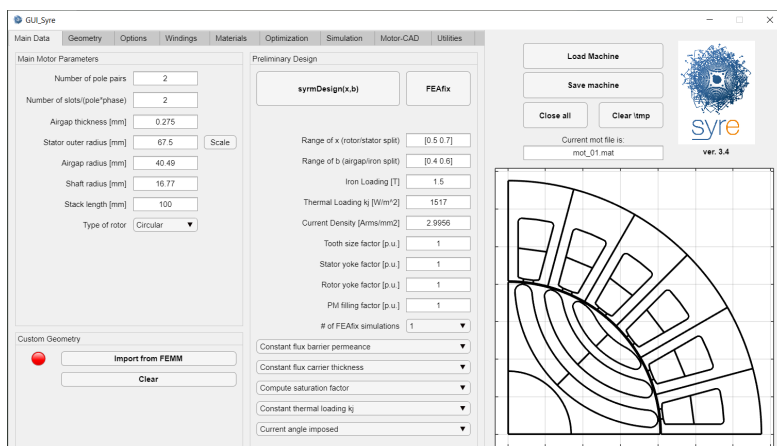


Figure 3.2: SyR-e main GUI.

The second interface, MMM GUI, on the other hand, allows loading the magnetic models for the machine under consideration, to evaluate MTPA and MTPV control trajectories, and to carry out model skewing and scaling. In the *Torque-Speed* tab, it is possible to evaluate both the operating limits of the machine, giving as input maximum voltage and current, and the efficiency maps in which it is possible to choose the type of control desired and include or not iron, mechanical and AC losses.

3.2 Add new Materials in SyR-e

For the work done in this thesis, three different materials were added to the SyR-e library: iron sheet NO27, used in both the benchmark motor and the motor designed with FeN magnets, and two different magnets, Niron GEN2, and N42UH.

3.2.1 Iron material: NO27

NO27 is a non-oriented electric steel with a nominal thickness of 0.27 mm . The parameters to be entered into SyR-e software to create the material model are:

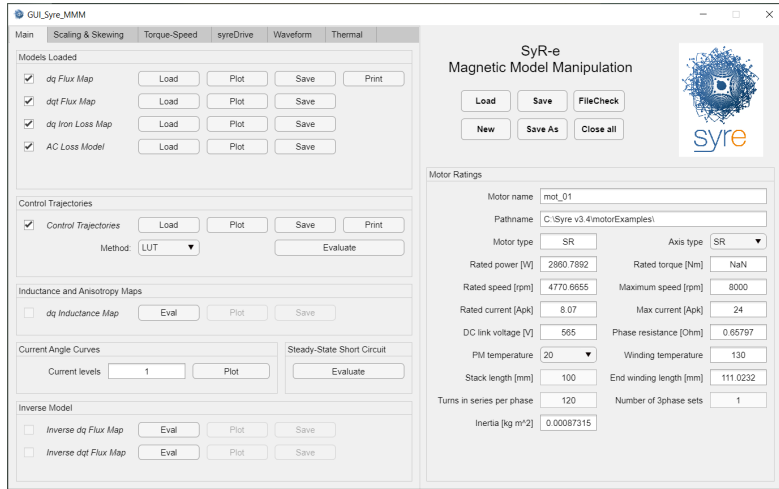


Figure 3.3: SyR-e MMM GUI.

yield strength, Young module, density, four coefficients for calculating iron loss and the BH curve. For the iron loss, SyR-e uses modified Steinmetz model (10), where iron loss are divided into two terms: hysteresis loss and eddy-current loss.

$$p_{Fe} = k_h f^\alpha B^\beta + k_e (fB)^2 \quad (10)$$

B is the flux density in the iron section, f is the frequency, k_e , α , β are hysteresis loss coefficients and k_e is eddy-current loss coefficient.

The coefficients in the equation were obtained by fitting the loss data from the manufacturer datasheet with Matlab app *Curve Fitter*. Fig. 3.4 shows the loss curves taken from the datasheet (red circles) and the surface area calculated using (10) to approximate them. The coefficients calculated and used are shown in Table 3.1.

Table 3.1: Steinmetz coefficients used.

α	1.1147
k_h	0.01196
k_e	2.8613 e-5
β	1.784

With regard to the introduction of the BH curve, it is needed to pay attention

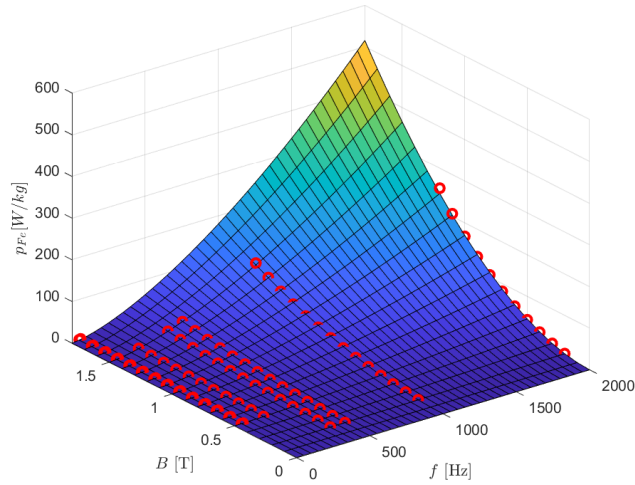


Figure 3.4: Datasheet iron loss (red circles) and interpolating surface (10).

to the maximum values of B for which you have the values. Generally, the data available from datasheets are limited to inductance values up to 1.8 T (as in this case) or slightly higher, but rarely to values that can guarantee complete saturation of the ferromagnetic material. In the absence of further information, if the material should work at higher B values, FEMM extrapolates the BH characteristic linearly, based on the slope of the last two known points. The extrapolated values are accurate only if the BH curve reaches the saturation zone where the slope of the curve is constant and equal to μ_0 (i.e. $J(H) = J_{sat}$). For this reason, the BH curve obtained from the datasheets must be first extrapolated to full saturation. The method used is described in [15] and uses the assumption that lamination sheets with the same density have the same J_{sat} . Fig. 3.5 shows the summary data of the material added in SyR-e.

3.2.2 Magnet material: N42UH

The magnet introduced is the sintered NdFeB magnet N42UH. The data to be entered in SyR-e for the creation of a new magnet are: density, conductivity, remanence, relative permeability, intrinsic coercivity, temperature to which these data relate and the thermal coefficients for remanence and coercivity. Fig. 3.6 shows the summary data of the material added in SyR-e.

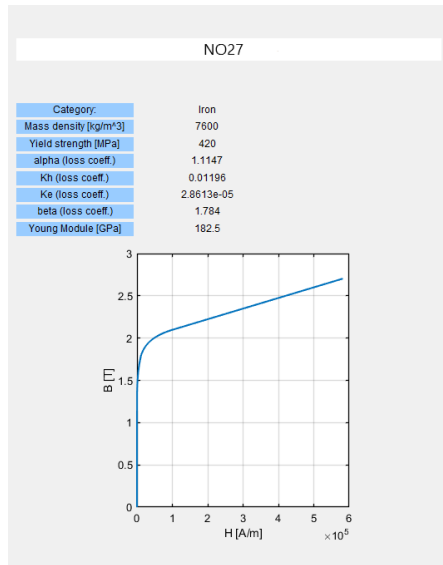


Figure 3.5: NO27 data in SyR-e.

3.2.3 Magnet material: Niron GEN2

The creation of the FeN magnet model is not as simple as that of N42UH. In fact, the BH characteristic of the Niron GEN2 magnet is non-linear in the second quadrant already at room temperature, unlike common RE magnets. Since SyR-e allows only linear characteristics to be entered, the BH curve was approximated with only the linear section and the H_{cJ} value was set equal to the limit of the linear section in order to "cut off" the characteristic before the knee point to be able to study demagnetization.

3.3 SyR-e and Demagnetization

Understanding how the demagnetization problem is handled in SyR-e is crucial, considering that demagnetization is one of the main problems in the use of FeN magnets. SyR-e during its simulations only uses the linear characteristic, the value of H_{cJ} only comes into play when performing demagnetization simulations: *Demagnetization Curve* and *Demagnetization Analysis*. The former allows, using an iterative procedure, to calculate the value of the current that demagnetizes 1% of the total volume of the magnet. Demagnetization Analysis, on the other hand, allows to choose the current value for which the volume percentage of the

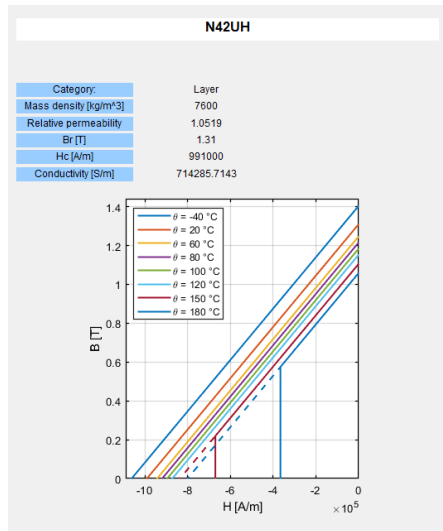


Figure 3.6: N42UH data in SyR-e.

demagnetized magnet is calculated. During these analyses, the conservative choice is made to consider all current in the $-d$ axis (against the magnets). FEMM software performs several FEA simulations and calculates the flux density values of the various points of the magnet mesh, if these are below the limit of the linear characteristic, SyR-e will consider that point of the magnet demagnetized.

It is important to emphasise, however, that in reality the situation is more positive because the current is never all in the $-d$ axis, except in particular high-speed flux weakening conditions. Moreover, even if a point of the magnet is found to be working beyond the linear line, this is not necessarily considered to be totally demagnetized, as it may be just beyond the limit and thus be affected by very slight demagnetization.

Demagnetization Analysis can also be used to study demagnetization under short-circuit conditions. SyR-e allows the estimation of the peak short-circuit current that could occur during a three-phase symmetrical short circuit. The simulation is called *HWC Short-Circuit Current* and the acronym HWC means 'Hyper-Worst-Case', because phase resistance and all other loss terms are neglected. Once the current value has been calculated, Demagnetization Analysis can be performed to assess the effect that this current would have on the magnets.

3.4 syrmDesign and FEAffix

The SyR-e software allows the preliminary design of a motor via *syrmDesign* functionality. This tool is accessible from the main GUI in the *Main Data* tab, in the *Preliminary Design* section (see Fig. 3.2). It was originally created for the design of SyR motors with constant iron flux density and thermal load. It allows a design plan to be calculated, using only analytical equations. For the magnetic design of the machine and the definition of the stator and rotor geometry, the peak torque at the maximum inverter current and the peak power at the maximum converter current and voltage required by the application are considered. The torque and power factor, and other parameters of interest, are plotted function of two dimensionless parameters shown in (11).

$$x = \frac{r}{R} \qquad b = \frac{B_g}{B_{Fe}} \qquad (11)$$

x is the rotor/stator radius ratio and b is the airgap/iron flux density ratio. Each point in this design plan represents a different motor and the best design can be selected, based on the desired performance and inputs. Over the years, the approach has been improved with the addition of the FEAffix algorithm, which allows analytical equations to be corrected via a few selected FEA simulations (the number of FEA simulations is selectable from the main GUI). Fig. 3.7 shows an example of a design plan in which there are also 3 different motors to see how the geometry changes as x and b vary. The green dots represent the 16 points in the plan (4×4 equispaced grid) where the 16 FEA simulations were carried out. The latest improvements concern PM motors and the extension of the *syrmDesign*/FEAffix approach to PMASynRM and IPM machines.

The design of these planes is based, as mentioned, on analytical equations. The d-axis is the main flux direction and therefore the iron core is designed according to the d-axis equations for both the stator and rotor. Fig. 3.8 shows the geometric parameters of a motor in the SyR case. The nomenclature and parameterisation logic does not change in the V-shape case. The size of the stator yoke l_y is determined as shown in (12).

$$l_y = \frac{R}{p} \cdot k_{ys} \cdot x \cdot b \qquad (12)$$

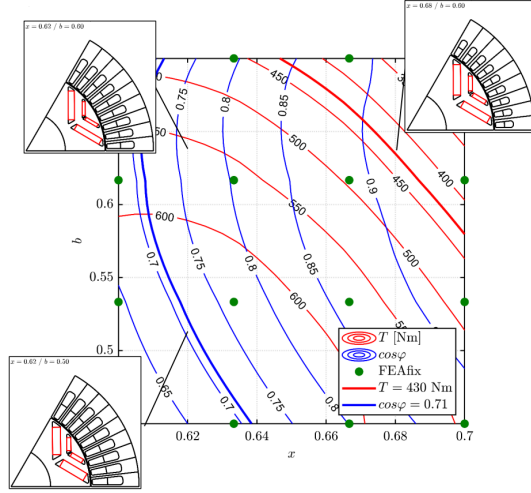


Figure 3.7: Example of a syrmDesign plane.

The reference condition $k_{ys} = 1$ refers to the case of a sinusoidal airgap flux density, imposing a yoke flux equal to half the pole flux. This is valid neglecting the presence of slot leakage flux. The tooth size is defined by the equation (13).

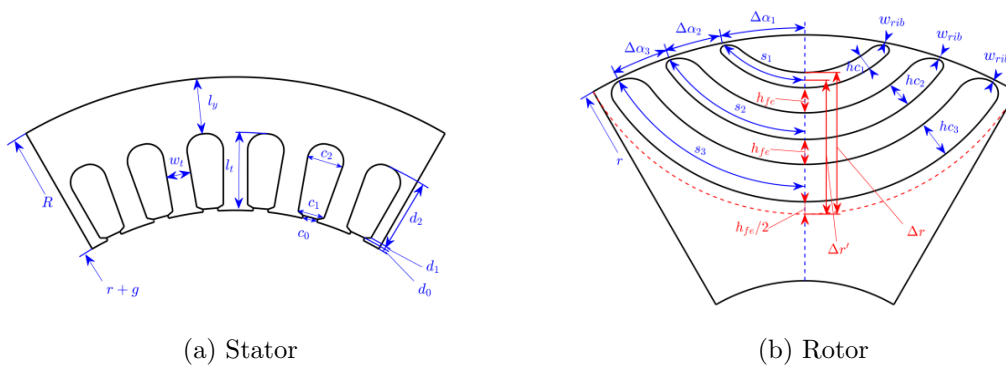
$$w_t = \frac{2\pi R}{6pq} \cdot k_t \cdot x \cdot b \quad (13)$$

The tooth size factor k_t defines the tooth size in relation to the yoke size. A value $k_t < 1$ is normally chosen to indicate that the tooth is more saturated than the back iron. As far as the size of rotor iron paths is concerned, the default design condition is that the sum of the flux carriers size ($l_r = \sum h_{Fe}$) equals the stator back iron size l_y . In (14), the rotor yoke factor k_{yr} is introduced to vary the rotor carriers' size with respect to the default condition.

$$k_{yr} = \frac{l_r}{l_y} \quad (14)$$

The parameters k_t , k_{ys} , k_{yr} can be set and changed in the main GUI where they are referred to as *Tooth size factor [p.u.]*, *Stator yoke factor [p.u.]* and *Rotor yoke factor [p.u.]*, respectively. Further information on how the torque and PF curves and the correction coefficients of the FEAfix are calculated can be found in [16].

The result of the FEAfix function will be a plot with the torque and PF curves



(a) Stator

(b) Rotor

Figure 3.8: SyR-e geometric parameters [16].

plotted on the xb plane. To access all other information not shown but contained within this file, simply save the figure in MATLAB Figure format and load it into the *syrmDesign Explorer* GUI (in Fig. 3.9) with the *Load Design Plane* button. This GUI is accessible from the *Utilities* tab in the main GUI and here it is possible to display many more variables on the plane, modify the number of turns N_s , the voltage V_{dc} , and the stack length, and above all draw and save the desired motor by giving the x and b values as input.

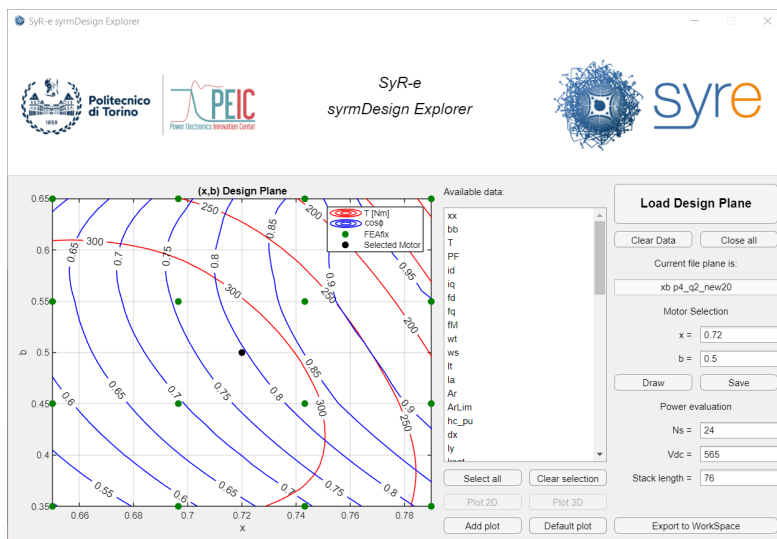


Figure 3.9: syrmDesign Explorer GUI.

4 Benchmark Motor Design

In order to compare the performance of FeN magnets when used in automotive applications, it is essential to have a reference motor, designed with RE PMs, with the same characteristics, especially in terms of torque, power, and size.

The benchmark search was based on the environmental sustainability and CO₂ reduction goal.

Since a particularly critical point of PMSMs motors with hairpin are AC losses, we wanted to evaluate different numbers of pins per slot. Once the ideal number of pins was chosen, a benchmark was designed to meet typical requirements for motors in automotive applications. These requirements are shown in Table 4.1 and the same requirements will then be used for the design with FeN magnets.

Table 4.1: Design targets.

Supply voltage [V]	400
Torque [Nm]	310
Maximum power [kW]	180
Outer stator diameter [mm]	230
Max active length [mm]	145
Max motor speed [rpm]	15000

4.1 Number of Pins/Slots and AC losses

As motor speed increases, the conductors are exposed to ever higher frequency alternating flux, leading to high induced eddy currents in the conducting material. This results in a non-uniform current density distribution over the conductor's cross-sectional area and in further losses, known as AC winding losses.

4.1.1 Types of Eddy Current Losses

There are four types of eddy current losses in electrical machine windings, illustrated in Fig. 4.1. This includes the skin effect, proximity effect, eddy current loss due to external field, and circulating current losses.

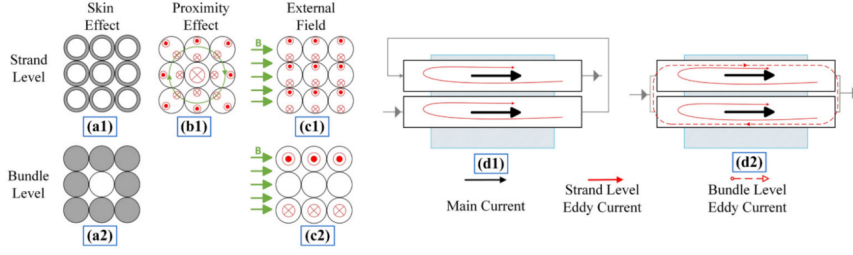


Figure 4.1: Different types of eddy current losses [17].

Basically, the skin effect is the non-uniform distribution of the current density in a conductor due to its own time-varying current. Regarding the proximity effect, the non-uniform distribution of the conductor current occurs due to currents in the adjacent conductors, as shown in Fig. 4.1(b1). A third type of loss is the eddy current loss due to the external magnetic field, which is simply demonstrated in Fig. 4.1(c1,c2). One last type of loss is the circulating current loss (Fig. 4.1(d1,d2)) in which two solid conductors are located inside a slot with the upper conductor facing less area of the ferromagnetic material. If the two conductors are connected in series, there will be a parasitic eddy current induced in the strand level due to the variation of the flux lines. Furthermore, if these conductors are connected in parallel there will be an additional circulating current at the bundle level. The main reason for this current is that the magnetic flux that is linked by the upper conductor is lower than the bottom one, resulting in a voltage difference between the two strands. One of the effective solutions to reduce this circulating current is the transposition of the strands so that each one is exposed to the same level of flux linkage.

In a single rectangular conductor with a height of h_c , width of w_c , and active length of l , the eddy current losses due to the external AC magnetic field can be expressed as in (15) [18].

$$P_e = B^2 \frac{\pi l \omega^2}{24 \rho} w_c h_c^3 \quad (15)$$

B is the magnitude (peak) of the sinusoidal external field, ω is the angular frequency, and ρ is the material resistivity. From the above equation, it can be seen that the conductor height is one of the parameters that most influences eddy current losses and that the pin most affected by the higher eddy current losses

will be the one adjacent to the airgap, where the flux density value is the highest. Therefore, reducing the height of the conductors certainly reduces the eddy current losses.

4.1.2 Hairpin Selection

Two motors were designed to assess how the machine's performance changes as the number of pins per slot varies. The two motors have the same 2D geometry shown in Fig. 4.2 while Table 4.2 shows the main characteristics.

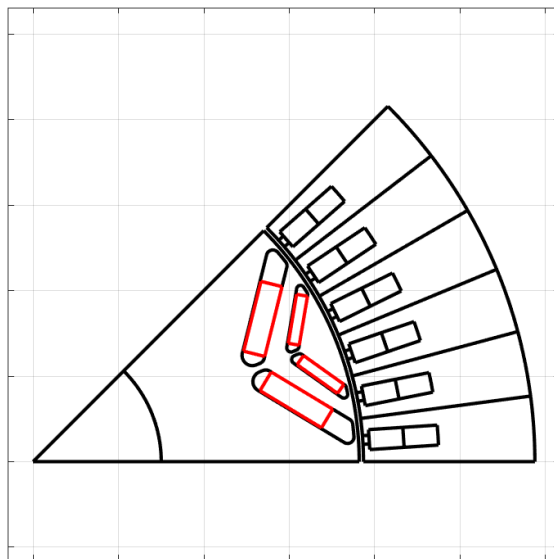


Figure 4.2: Benchmark cross-section.

The two machines have different numbers of pins per slot (6 pins and 8 pins), and the same phase current (572 A) but different active lengths to achieve the same performance. The 6-pin motor has an active length of 95 mm and a number of turns in series per phase equal to 16 (2 parallel paths). In contrast, the 8-pin motor has an active length of 145 mm and a number of turns in series per phase equal to 24 (4 parallel paths). The feasibility of this winding has been verified.

The torque limits are shown in Fig. 4.3. It can be seen that the two motors have the same maximum torque and that the 8-pin motor has a higher base speed (and therefore power) due to the different winding, and fewer turns in series per phase which are not balanced by the longer length of the machine.

Table 4.2: Comparison of 6-pin and 8-pin motors.

		6-pin	8-pin
Torque	[Nm]	310	310
Base Power	[kW]	145	162
Stack length	[mm]	95	145
Stator outer diameter	[mm]	230	230
Current density	$[A_{rms}/mm^2]$	26.9	15
Phase current	$[A_{pk}]$	572	572
Pins/slot		6	8
Parallel path		2	4

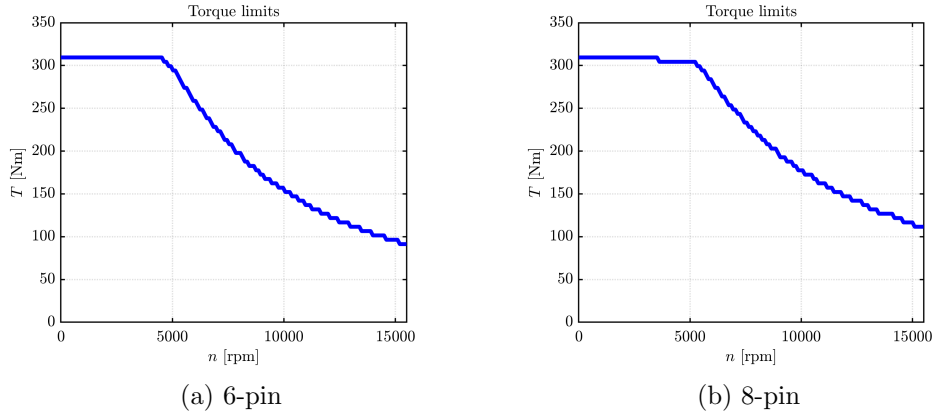


Figure 4.3: Torque limits: 6-pin vs 8-pin.

Whereas, Fig. 4.4 shows the comparison of Joule losses in the stator windings, where the 8-pin motor shows much lower values, despite being a much longer motor. Table. 4.3 allows a better visualization of the comparison because the DC and AC loss values at a vehicle speed of 120 km/h are shown separately. Since beyond the base speed the motors behave differently, i.e. different torque limit values, data are shown for the 8-pin motor at both its own torque limit and those of the 6-pin motor. The 8-pin motor presents lower values of both DC and AC losses, while the former are mainly due to the different number of parallel paths, the latter confirm the lower losses per eddy current for the 8 pins/slot case.

To assess the overall efficiency trend, the efficiency maps of the two motors

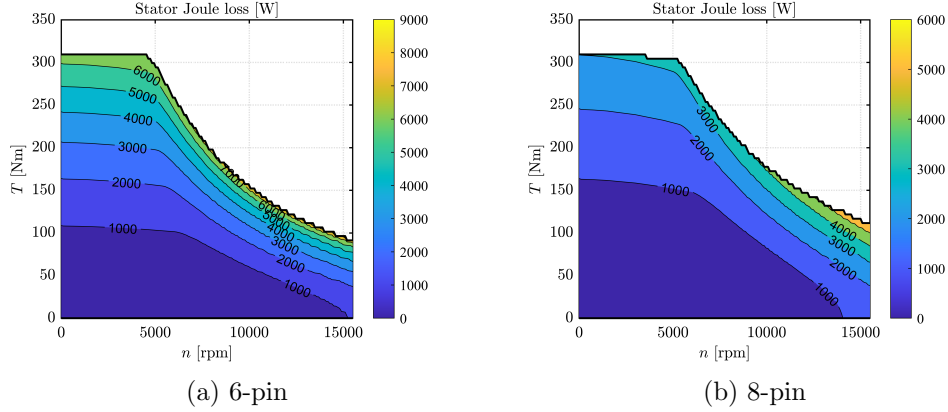


Figure 4.4: Stator Joule losses: 6-pin vs 8-pin.

Table 4.3: Joule losses comparison @ 120 km/h

		6-pin	8-pin
		162 Nm	182 Nm
DC losses [W]	@ $T_{lim,6-pin}$	5677	2240
	@ T_{lim}		2730
AC losses [W]	@ $T_{lim,6-pin}$	1500	928
	@ T_{lim}		1131
DC+AC losses [W]	@ $T_{lim,6-pin}$	7177	3168
	@ T_{lim}		3861

are shown in Fig. 4.5. The 8-pin shows higher efficiencies for higher speeds but especially for high torque values. However, when analyzing some interesting points of work for the application, the situation changes. Table 4.4 shows the efficiency values for two different vehicle speeds, 80 - 120 km/h, for three different torque values, 20 - 30 - 40 Nm. 6-pin motor shows higher efficiency values at almost all points.

The 6-pin motor has higher efficiencies at almost all operating points of interest and this advantage is accompanied by an additional advantage in terms of materials. Table 4.5 reports and compares the mass of the materials involved. 6-pin motor due to its shorter stack length has a significantly lower total weight (29.08 kg vs 44.71 kg) but above all a lower quantity of magnets (1.39 kg vs 2.14 kg).

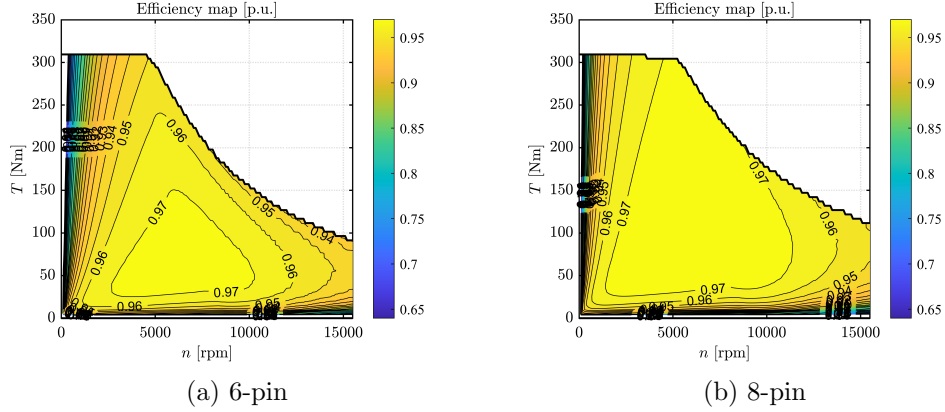


Figure 4.5: Efficiency map: 6-pin vs 8-pin.

Table 4.4: Efficiency points: 6-pin vs 8-pin.

	6-pin	8-pin	8-pin vs 6-pin	
20 Nm	0.964	0.958	- 0.59%	
80 km/h \approx 6411 rpm	30 Nm	0.971	0.969	- 0.21%
	40 Nm	0.973	0.973	+ 0.00%
120 km/h \approx 9623 rpm	20 Nm	0.962	0.955	- 0.66%
	30 Nm	0.968	0.967	- 0.15%
	40 Nm	0.971	0.972	+ 0.06%

For these reasons, it was decided to design the reference motor with 6 pins/slots and 2 parallel paths.

4.2 Initial Design Improvement

In order to achieve the desired power target, with the possibility of increasing the current density, the active length of the motor was reduced to 75 mm, bringing the phase current to 717 A_{pk} (current density $33.7 A_{rms}/mm^2$). In this way, it is also possible to pursue the goal of greater motor environmental sustainability because the volume of material used is reduced. The L75 motor was created and compared with the previous design that we will call L95. The two motors have the same geometrical and winding characteristics, except for the active length and current.

Table 4.5: Materials: 6-pin vs 8-pin.

	Material		6-pin	8-pin
Stator core	NO27	[kg]	14.86	22.93
Rotor core	NO27	[kg]	9.01	13.90
Windings	Copper	[kg]	3.82	4.74
Magnets	N42UH	[kg]	1.39	2.14
Total motor mass		[kg]	29.08	43.71

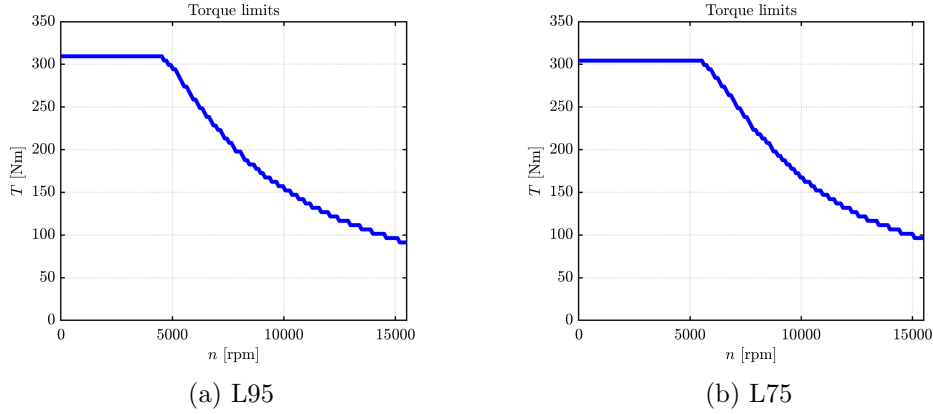


Figure 4.6: Torque limits: L95 vs L75.

As in the case of the previous comparison, torque limits graphs (in Fig. 4.6) and efficiency maps (in Fig. 4.7) are shown.

With regard to the first comparison, it can be seen that the two motors have the same maximum torque value with L75 having a higher base speed due to its shorter length. Unlike the previous case, there is no difference in the winding in this comparison. As far as the comparison of efficiency maps is concerned, L75 has the flatter and longer maximum efficiency zone, i.e. higher efficiencies for high speeds and lower efficiencies for high torques. Again, efficiencies at six different operating points are compared and shown in Table. 4.6. L75 has higher efficiencies at all these operating points as well as a considerable advantage in the materials used, the comparison can be found in Table. 4.7.

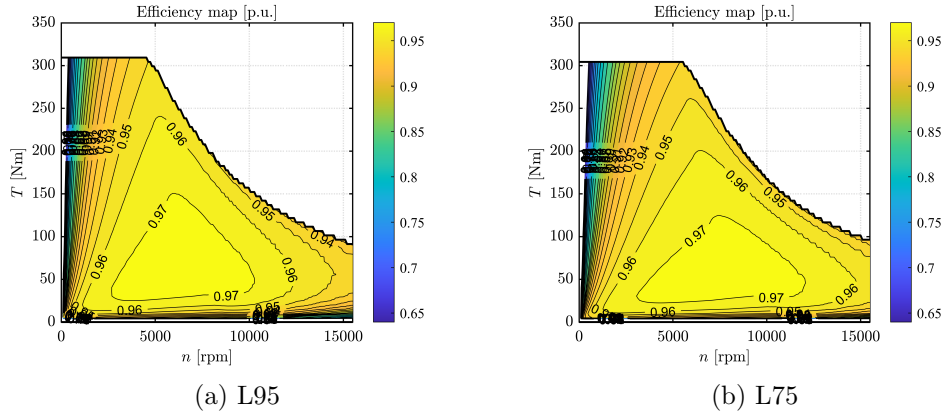


Figure 4.7: Efficiency map: L95 vs L75.

Table 4.6: Efficiency points: L95 vs L75.

		L95	L75	L75 vs L95
80 km/h \approx 6411 rpm	20 Nm	0.964	0.968	+ 0.42%
	30 Nm	0.971	0.973	+ 0.18%
	40 Nm	0.973	0.974	+ 0.01%
120 km/h \approx 9623 rpm	20 Nm	0.962	0.964	+ 0.23%
	30 Nm	0.968	0.971	+ 0.25%
	40 Nm	0.971	0.974	+ 0.26%

Table 4.7: Materials: L95 vs L75.

	Material		L95	L75
Stator core	NO27	[kg]	14.86	12.01
Rotor core	NO27	[kg]	9.01	7.28
Windings	Copper	[kg]	3.82	4.06
Magnets	N42UH	[kg]	1.39	1.12
Total motor mass		[kg]	29.08	24.47

4.3 Selected Benchmark: L75

For the reasons shown, L75 motor was the chosen benchmark, whose main characteristics are given in Table 4.8 and the geometry cross-section in Fig. 4.2.

Table 4.8: L75 summery data.

Slots		48
Pole pairs		4
Pins per slot		6
Stack length	[mm]	75
Outer stator diameter	[mm]	230
Torque	[Nm]	304
Maximum Power	[kW]	185
Current Density	$[A_{rms}/mm^2]$	33.7
Phase Current	$[A_{pk}]$	717

This motor will be the reference for the design with the FeN RE-free magnets, described in the next chapter, and the comparison of which is given in the last chapter. Fig. 4.8 also shows a demagnetization study for the L75 motor to allow a comparison with FeN magnets, whose main problem is demagnetization. The graph shows two curves for 5 different temperature values: the demagnetization current $I_{demag,1\%}$ (in blue) calculated with the SyR-e *demagnetization Curve* function and the short-circuit current $I_{cc,HWC}$ (in orange) calculated with the SyR-e *HWC Short-Circuit Current* function, taking the point at base speed and maximum torque as the pre-fault point.

It can be seen that the current tolerated by the magnets is much higher than the rated motor current and also much higher than the short-circuit currents for PM temperatures below 100 °C. This means that if the temperature is higher than 100 °C risk of demagnetization occurs if Active Short Circuit (ASC) is performed.

As we shall see, this will not be the case with FeN magnets.

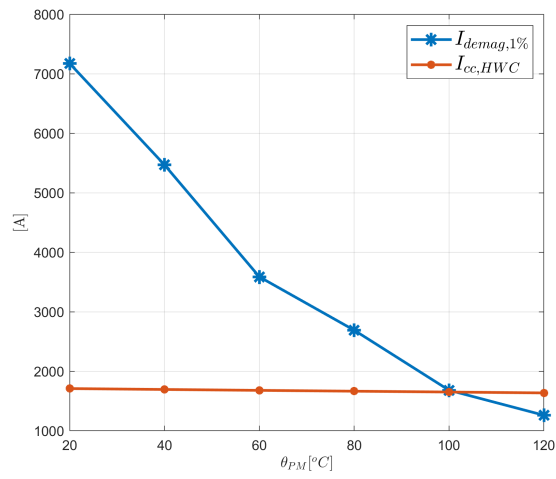


Figure 4.8: Demagnetization current and HWC three-phase short-circuit current.

5 Design of FeN IPM motor using SyR-e

The preliminary design of the motor with FeN magnets was approached using the `syrmDesign` tool implemented on SyR-e and described in Chapter 3.4. The design targets are the same as those used for the benchmark motor design and are shown in Table 4.1. Since the main limitation of these magnets is demagnetization and `syrmDesign` did not allow the demagnetization problem to be taken into account during initial design, a new approach was developed based on the paper "*Design of Ferrite-Assisted Synchronous Reluctance Machines Robust Toward Demagnetization*" [19] and implemented in `syrmDesign` tool.

As FeN magnets are still a developing technology, studies on ferrites are a good starting point, as they have similar or slightly higher coercivity values. However, it should be noted that it is not possible, during the design phase, to treat FeN magnets as if they were hard ferrites. In fact, a substantial difference is the remanence value. With values much higher than those of ferrites (and even higher than those of NdFeB magnets), there is a risk of saturating the rotor iron if you try to use FeN PMs in a motor designed to work with ferrites. Multi-barrier geometries with more than two barriers will therefore be more difficult to realize. Such high remanence values represent the advantage, and not the disadvantage, of FeN magnets over ferrites, but a different design must be considered and developed.

For the design, it was decided to keep a V-shape rotor and study how the geometry influences demagnetization by varying the number of poles, slots, and barriers. From early designs, it became clear that it was not possible to realize a design capable of achieving the torque and size requirements with nominal current values that had a significant margin over the demagnetization limit current. Therefore, the goal was to find a design capable of reaching the requirements with the smallest possible demagnetization value. This means that during normal operation there will be a volume of the magnet, which we want to be as small as possible, that will work beyond the lower limit of the linear section of the characteristic and consequently on a recoil line with a lower remanence value.

Since SyR-e cannot use non-linear characteristics to describe the behavior of magnets, it is not possible to assess the real demagnetization and dynamic behavior of the motor. For these reasons, in this chapter, we will focus on evaluating demagnetization with the tools available in SyR-e (described in Chapter 3.3), i.e.

estimating it in terms of the percentage of magnet volume that exceeds the limit imposed for the linear characteristic.

After introducing the theory on which the procedure is based, different cases are studied and compared with varying the number of poles and current density, first for the 1V-shape case and then for the 2V-shape case. Finally, a sensitivity study is carried out, for the k_t , k_{ys} , k_{yr} parameters introduced in Chapter 3.4, for the case of interest. To conclude, a recap of the characteristics of the final design is presented.

5.1 Reference Literature

Among the topics available in the literature, the study of the design of ferrite-assisted synchronous reluctance (FASR) machines, with focus on the pivotal aspect of avoiding irreversible demagnetization, certainly represents an interesting starting point for defining a design strategy. Even if in our case we want to design an IPM motor and not a SynRM, the theory on how geometry influences demagnetization is equally applicable. In particular, the work carried out by Vagati et al. [19] provides some geometric rules to achieve a robust design against demagnetization and equations to calculate the electrical load limit corresponding to demagnetization.

The reference geometry considered in this work is shown in Fig. 5.1 and represents a rectified pole of an FASR machine with distributed windings. The fundamental geometrical parameters shown are:

- the airgap thickness g ;
- the pole pitch a ;
- the stator teeth length l_t ;
- the pitch of the k -th rotor “slot” $\Delta\xi_k$;
- half the width of the k -th layer S_k and its thickness l_k ;

The dq axes are defined according to the SR-style, being a PMASynRM.

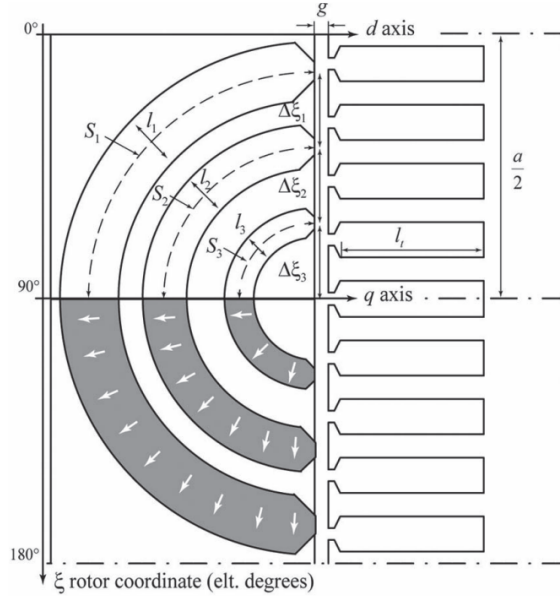


Figure 5.1: Paper reference geometry [19].

Regarding the number of rotor flux barriers and their shape, different choices are possible, since the theory was developed to deal with any type of multilayer rotor structure.

Note also that the rectified geometry shown is more similar to the actual pole of a rotating machine when it has a high number of pole pairs while the model is less accurate for a low number of pole pairs. This is because the curvature of the pole reduces the amplitude of the S_{123} barrier compared to Fig. 5.1. The smaller barrier width produces greater isolation along the q-axis than predicted by the model. Therefore, the model is more accurate for high pole numbers and tends to be conservative when applied to lower pole numbers, in terms of isolation (i.e. stiffness against demagnetization). Since in our study, we will be analyzing machines with a not particularly high number of poles, we expect to find a more conservative, but still useful, model to guide us towards the optimal direction.

The key equation in [19] is (16) and indicates the q-axis electrical load (against the PMs) that can be tolerated by the magnets.

$$A_{q,irr} = \frac{\pi B_r l_{a,pu}}{4 \mu_0 f_{qn}} \cdot \left(1 - \frac{B_{m,irr,pu}}{B_{m0,pu}} \right) \quad (16)$$

Where:

- μ_0 is the vacuum magnetic permeability;
- $l_{a,pu}$ is the total insulation, sum of all l_k [m], in p.u. of $a/2$;
- f_{qn} is the top level of the p.u. stator MMF, for the case of n layers (value close to 1);
- B_r is the PM remencance value [T];
- $B_{m,irr,pu}$ is the lower limit of reversible demagnetization [T], in p.u. of B_r ;
- $B_{m0,pu}$ is the flux density in the magnets at no-load [T], in p.u. of B_r .

The term in brackets says that $A_{q,irr}$ is a function of the margin between the material property $B_{m,irr,pu}$ and the no-load flux density $B_{m0,pu}$. If $B_{m0,pu}$ is too close to $B_{m,irr,pu}$, then the feasible load tends to zero and the torque with it. Basically, $B_{m0,pu}$ in (16) summarises the geometry, while B_r and $B_{m,irr,pu}$ summarise the combination of PM quality and operating temperature. Using the equation (17) provided in the same paper, it is then possible to relate the electrical load to the machine's main geometrical parameters.

$$B_{m0,pu} = \frac{1}{1 + \frac{S_1 g}{l_a a} \frac{2\pi}{\Delta\xi_r} \sin(\Delta\xi_r/2)} \quad (17)$$

Equation (17) shows that high values of a/g (i.e. small airgaps per unit), together with large magnetic isolations l_a , keep $B_{m0,pu}$ close to one per unit. Hence, the PMs working flux density at no-load stays close to the remanence value, and it means that the magnets are not heavily loaded, at least at zero current. Having high a/g ratios means that the airgap is thin relative to the pole pitch, and since the minimum limit on the size of the airgap is given by manufacturing limits, to increase the value of the ratio it is necessary to increase the value of the pole pitch and thus decrease the number of poles. Equations (16) and (17) have therefore been added to the `syrmDesign` tool. Fig. 5.2 shows how the geometric parameters presented in the paper are translated to the case of a V-shaped rotor and implemented in the tool.

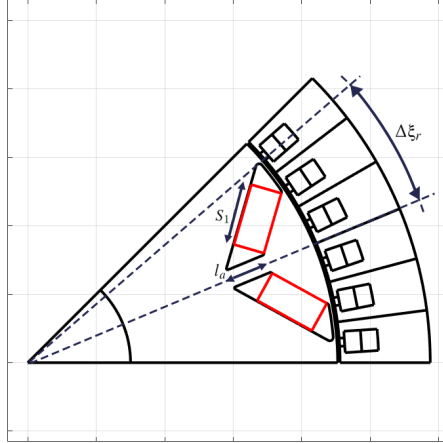


Figure 5.2: Geometry parameters in the V-shape case.

In the following, the different geometries will be analyzed taking into account the value of $A_{q,irr}$ (hereafter referred to as $A_{d,irr}$ because the PM-style convention of axes will still be used). In particular, what really interests us is not only to have a high value of $A_{d,irr}$ but to evaluate the margin between $A_{d,irr}$ and the electrical load A_d , calculated with the formula (18), at the design point with maximum torque and base speed. To this end, the characteristic A_{diff} (19), given by the difference between the two, will be plotted and used as a useful parameter to define the demagnetization resistance of the analyzed machines.

$$A_d = \frac{\pi}{2} \cdot \frac{F_d}{a} \qquad F_d = \frac{3}{\pi} \cdot k_w \cdot \frac{N_s}{p} \cdot I_d \qquad (18)$$

Where:

- k_w is the winding factor;
- N_s is the number of turns in series per phase;
- p is the number of pole pairs;
- I_d is the d-axis current component.

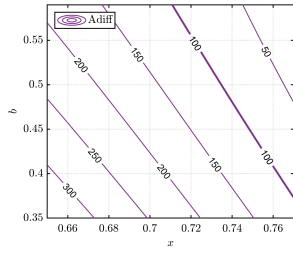
$$A_{diff} = A_d - A_{d,irr} \qquad (19)$$

Ideally, to secure the magnets against demagnetization, we would like to ensure that $A_d < A_{d,irr}$ (and thus $A_{diff} < 0$) for all possible magnet temperatures. But in our case, as we shall see, due to both the weak behavior of FeN magnets against demagnetization and the conservative analysis used when applying these formulae to our investigation, it will not be possible to guarantee $A_{diff} < 0$ but we will just achieve the desired targets by minimizing A_{diff} .

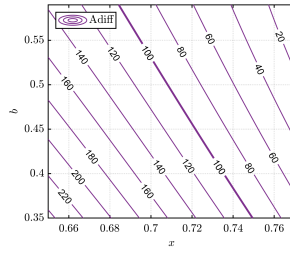
5.2 1V-shape Rotor Geometry

Initially, the geometry with a single barrier (1V-shape) was evaluated in terms of number of poles, slots, and current density. As a first design choice, the airgap thickness is decreased compared to the one chosen for the benchmark, and this value will also be kept in the 2V design. In fact, as explained above, high a/g ratio values keep the magnets not heavily loaded at no-load. Furthermore, it soon became clear that the electrical load values had to be much lower than those used in the benchmark in order to design motors that would not totally demagnetize the magnets. Consequently, a much lower electric load requires a considerably longer active length of the motor than the benchmark, not forgetting that the maximum target length is 145 mm.

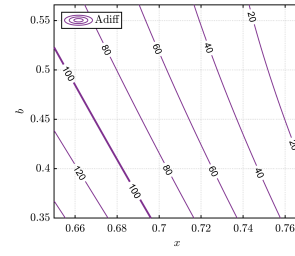
Fig. 5.3, 5.4 and 5.5 show the A_{diff} characteristics in the xb planes for the 6-, 8- and 12-pole cases respectively, for three values of current density: 20, 15, 10 A/mm². In all cases, a number of slots/pole/phase q equal to 2 was considered. As can be seen, with decreasing current density, the characteristics move in the low left direction, allowing the characteristics with lower A_{diff} values to emerge in the top-right plane. The 100 A/mm curve is highlighted in all planes in order to better visualize this trend. However, it must be emphasized that as the current density decreases, the contours of the torque also move in the same way as the A_{diff} curves. Increasing the active length, however, allows the torque contours to move in the opposite direction. But if the value of the active length is already at its maximum, decreasing the current density will bring no advantage to demagnetization because, as explained above, the two curves move together.



(a) 20 A/mm²

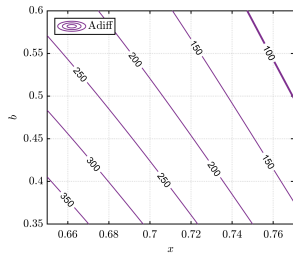


(b) 15 A/mm²

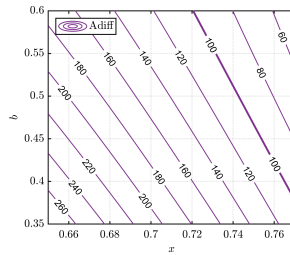


(c) 10 A/mm²

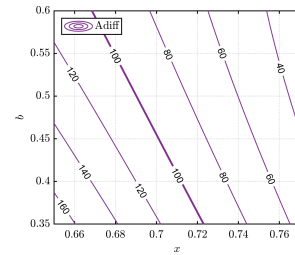
Figure 5.3: p3-q2 1V: A_{diff} vs current density.



(a) 20 A/mm²

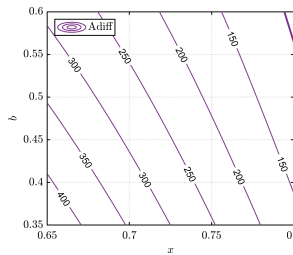


(b) 15 A/mm²

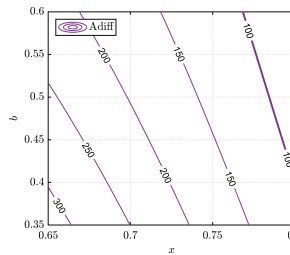


(c) 10 A/mm²

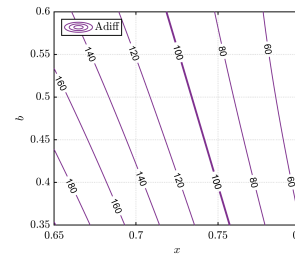
Figure 5.4: p4-q2 1V: A_{diff} vs current density.



(a) 20 A/mm²



(b) 15 A/mm²



(c) 10 A/mm²

Figure 5.5: p6-q2 1V: A_{diff} vs current density.

5.2.1 6-pole Case

Starting with the 6-pole case, Fig. 5.6 shows on the left the xb plane with the torque and A_{diff} contours in the 20 A/mm² case and with an active length at the max length target value of 145 mm.

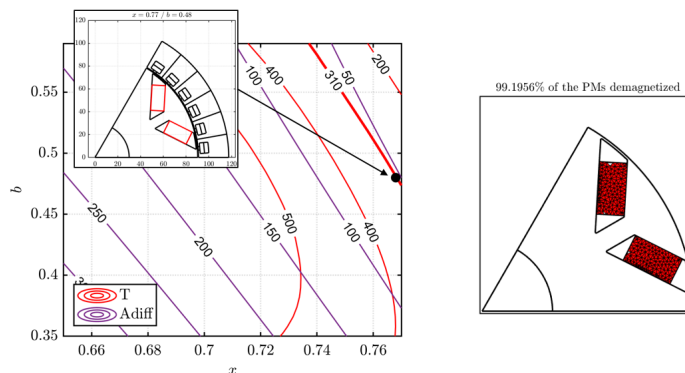


Figure 5.6: p3-q2 1V 20 A/mm²: xb plane design (on the left) and Demagnetization Analysis result (on the right).

The target curve of 310 Nm is above the value of $A_{diff} = 50$ A/mm and the point indicated by the black dot marks the design shown in the same figure, where $x = 0.768$ and $b = 0.48$. This motor has the desired torque and the minimum A_{diff} value. Increasing the active length would allow us to shift the 310 Nm curve to the right while leaving the A_{diff} curves unchanged and thus achieve lower values of A_{diff} which means better demagnetization behavior. However, in this case, we have already reached the maximum length. That point (x,b) in the plane needs approximately 8500 Ampere-turns. A feasible value of turns in series per phase N_s with this pole-slot combination is 12. With this value, the base speed will be 6800 rpm (dc-link voltage 400 V) and the phase current 700 A_{pk}. The value of N_s has been chosen in such a way to have a base speed close to the target base speed of 5500 rpm. The choice of this value has no influence on the demagnetization phenomenon, in which only the Ampere-turns value comes into play.

Unfortunately, as can be seen in Fig. 5.6 on the right, the result of the Demagnetization Analysis indicates that almost the entire volume of the magnet (99.2%) would be working beyond the limit of the linear characteristic. As already explained, this analysis assumes that the current of 700 A_{pk} is all in the -d axis

(conservative case) and the red area does not indicate the volume of the magnet totally demagnetized, but only the volume of the magnet working at a flux density below the linear limit, despite the title SyR-e gives to the image. Nevertheless, this result is obviously unacceptable.

Since in the previous case, where the current density was 20 A/mm^2 , we have already reached the maximum acceptable machine length value, it is not possible to achieve lower A_{diff} values by decreasing the current density. In fact, as can be seen in Fig. 5.7 for the case of 15 A/mm^2 , keeping the length constant also the torque curves translate and the torque contour at 310 Nm is always found beyond the value of $A_{diff} = 50 \text{ A/mm}$. Therefore it is not possible to reach the torque target, taking into account the limitation on the active length, with an acceptable demagnetization for the 1V 6-pole case.

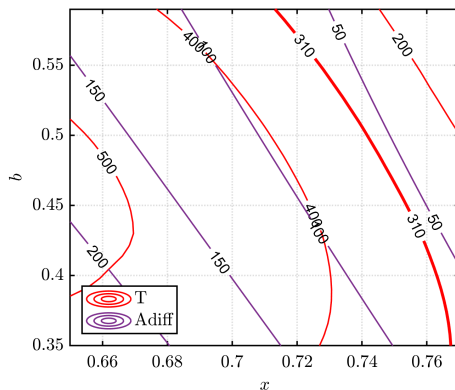


Figure 5.7: p3-q2 1V 15 A/mm^2 xb plane: Torque and A_{diff} .

5.2.2 8-pole Case

For the 8-pole case, we can see from Fig. 5.4 that 10 A/mm^2 is the only current density value that allows A_{diff} contours of less than 50 A/mm in the xb plane. However, Fig. 5.8 shows that the target torque contour 310 Nm for the active length equal to 145 mm is above the value of 60 A/mm . The design shown in the figure represents the motor at 310 Nm and minimum A_{diff} . As already observed in the 6-pole case, an A_{diff} value greater than 50 causes the magnets to work beyond the linear limit. So in this case, where A_{diff} is greater than 60 A/mm ,

the demagnetization behavior will be worse and this is confirmed by the Demagnetization Analysis simulation result shown in the same figure on the right. The simulation in this case was carried out with $N_s = 16$ (base speed 5600 rpm) and consequently the current value is $570 A_{pk}$. Thus, even in this case, torque target, active length target, and demagnetization cannot be met simultaneously.

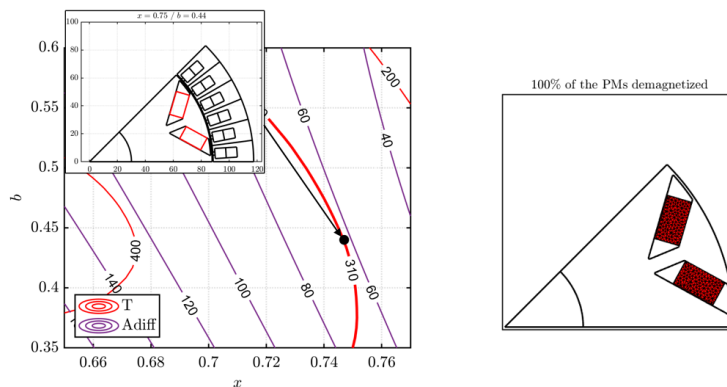


Figure 5.8: p4-q2 1V 10 A/mm²: xb plane design (on the left) and Demagnetization Analysis result (on the right).

5.2.3 12-pole Case

Also for the 12-pole case, it can be seen from Fig. 5.12 that the 10 A/mm² case is the only plane that has points with $A_{diff} < 60 A/mm$. As we have already seen, however, values above 50 A/mm do not allow for acceptable designs. For the sake of completeness, Fig. 5.9 also shows the best design for the 12-pole 10 A/mm² case and active length 145 mm. The motor needs about 9000 Ampere-turns so choosing $N_s = 18$ (base speed 5000 rpm) the current needed to produce the torque will be about $500 A_{pk}$. As can be expected, the result is not acceptable in this case either.

5.2.4 Summary and Conclusions

The 1V-shape geometry is far from achieving the torque and demagnetization targets without exceeding the target settled on the maximum active length. A summary of the characteristics of the possible designs shown above is given in

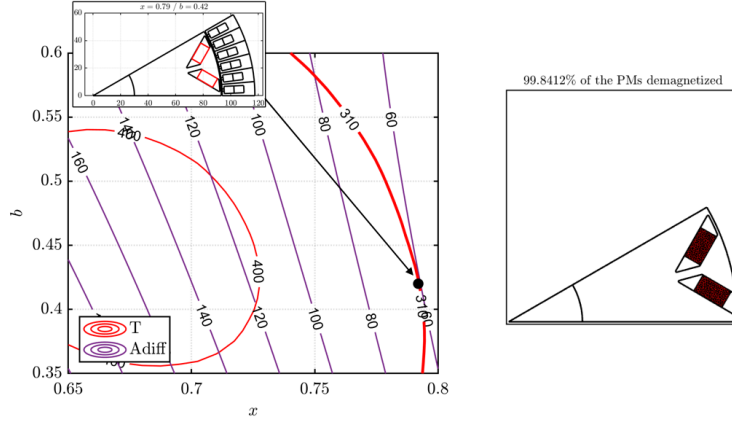


Figure 5.9: p6-q2 1V 10 A/mm²: xb plane design (on the left) and Demagnetization Analysis result (on the right).

Table 5.1. All three solutions presented fail to reach the torque target without pushing the magnets to work beyond the linear section. The 8-pole solution seems to be the best of the three because it is the only one to present points in the xb plane with A_{diff} values less than 40 A/mm. The max length target, however, does not allow, even in this case, to go below $A_{diff} = 60$ A/mm. If a 1V geometry were to be mandatory, the only solution to improve demagnetization behavior would be to further extend the machine (or vice versa, reduce the torque target), but this would lead to machines that are not very competitive for state-of-the-art motors.

Table 5.1: 1V-shape best designs.

		p3-q2	p4-q2	p6-q2
Current density	[A/mm ²]	20	10	10
Active length	[mm]	145	145	145
N_s		12	16	18
Torque	[Nm]	310	310	310
Base speed	[rpm]	6800	5600	5000
Phase current	[A _{pk}]	700	570	500
Demag @ ph. current	[%]	99.2	100	99.8

5.3 2V-shape Rotor Geometry

After analyzing the possibilities provided by the 1V-shape geometry, we moved on to study the 2V-shape case. Theoretically, this increases the flux of the magnets and thus decreases the current required to obtain the desired torque, decreasing the possibility of demagnetization. Furthermore, increasing the number of barriers means increasing the total magnetic isolation in the d-axis l_d , given by the sum of the thickness of each barrier, which helps to keep $B_{m0,pu}$ close to one per unit, as expressed by equation (17). This is confirmed by Fig. 5.10, 5.11 and 5.12 in which the A_{diff} characteristics are shown, as done previously for the 1V-shape case. The improvement is especially visible for the 6- and 8-pole cases, whereas for the 12-pole case, the characteristic does not particularly improve, and this is why the 12-pole case is not investigated further.

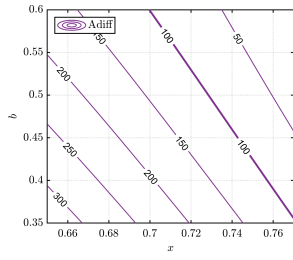
5.3.1 6-pole Case

For the 6-pole case, it is possible to note that for the first time, the curve $A_d = A_{d,irr}$, i.e. $A_{diff} = 0 \text{ A/mm}$, is visible on the xb plane for the 15 and 10 A/mm^2 current density cases. Starting, however, with the 20 A/mm^2 case, Fig. 5.13 shows on the left, as for the 1V-shape case, the design plane in which the 310 Nm torque curve for an active length of 145 mm is highlighted.

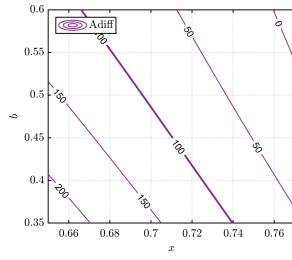
The target torque is slightly above the $A_{diff} = 30 \text{ A/mm}$ contour and the black dot marks the point in the xb plane where the torque is equal to the target torque and minimizes the A_{diff} value. Note that again, this point in the plane requires approximately 8500 Ampere-turns, and choosing $N_s = 18$ (base value 4800 rpm) means a phase current of 470 A.

On the right of the same figure, you can see the result of the Demagnetization Analysis, which indicates that the percentage of the magnet volume that would work beyond the linear section is only 0.48%, despite $A_{diff} = A_d - A_{d,irr} = 30 \text{ A/mm}$. This demonstrates that, as mentioned in Chapter 5.1, the model is conservative when applied to machines with low pole numbers. The reported design is certainly interesting and, having reached the maximum value of active length, a reduction in current density brings no advantage from the demagnetization point of view, as can be seen in Fig. 5.14 for the 15 A/mm^2 case.

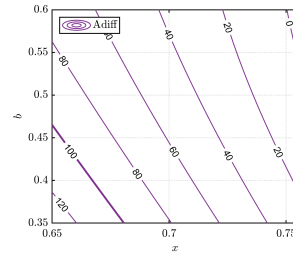
Therefore the value of $A_{diff} = 0 \text{ A/mm}$, even if present in the plane, is not



(a) 20 A/mm²

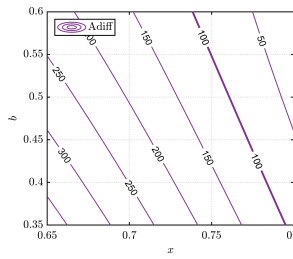


(b) 15 A/mm²

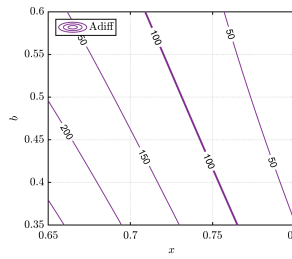


(c) 10 A/mm²

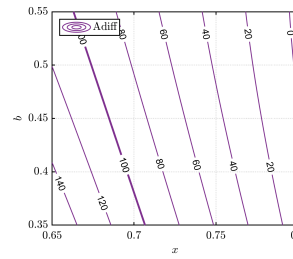
Figure 5.10: p3-q2 2V: A_{diff} vs current density.



(a) 20 A/mm²

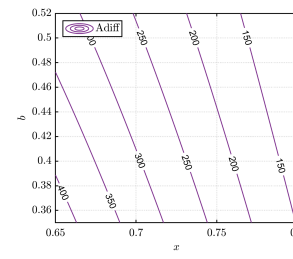


(b) 15 A/mm²

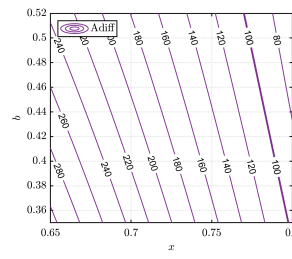


(c) 10 A/mm²

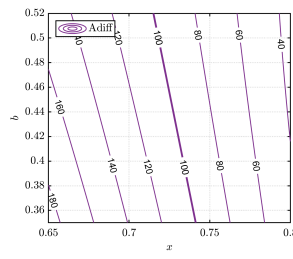
Figure 5.11: p4-q2 2V: A_{diff} vs current density.



(a) 20 A/mm²



(b) 15 A/mm²



(c) 10 A/mm²

Figure 5.12: p6-q2 2V: A_{diff} vs current density.

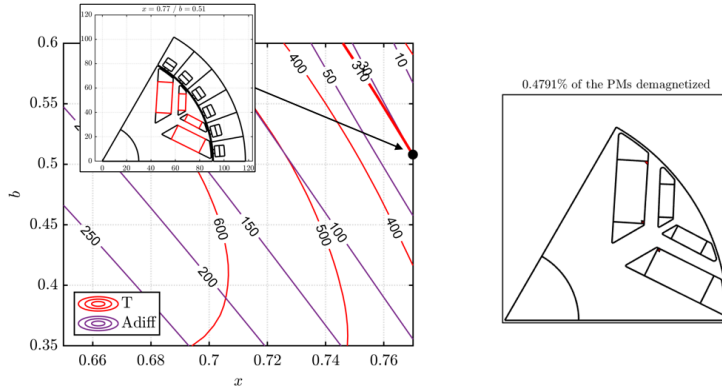


Figure 5.13: p3-q2 2V 20 A/mm²: xb plane design (on the left) and Demagnetization Analysis result (on the right).

achievable with our target on the max active length.

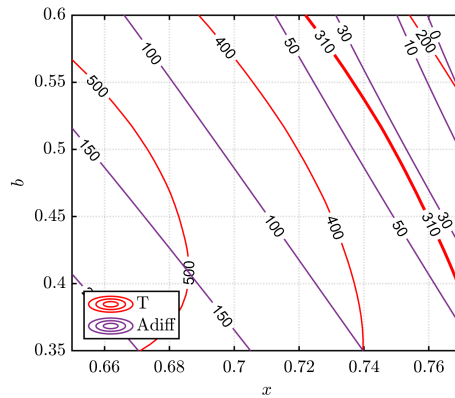


Figure 5.14: p3-q2 2V 15 A/mm² xb plane: Torque and A_{diff} .

5.3.2 8-pole Case

For the 8-pole case, in Fig. 5.15 it is possible to see the xb plane for the 20 A/mm² case, in which the 310 Nm contour is highlighted for an active length of 145 mm.

The 310 Nm and 30 A/mm curves do not intersect because they are close to the boundary value of the plane $x = 0.8$ and only in this case a decrease in current density helps demagnetization even though we have already reached the maximum

length target. This is because, even if the characteristics translate together, in this way the point where the two curves meet is located into the xb plane.

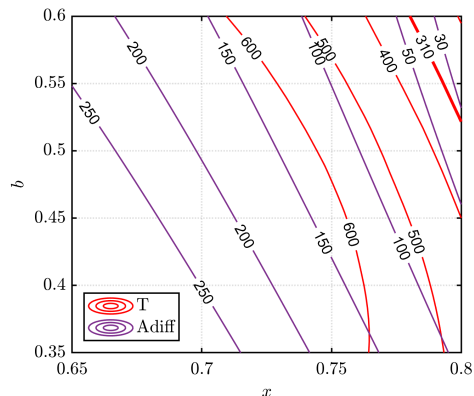


Figure 5.15: p4-q2 2V 20 A/mm² xb plane: Torque and A_{diff} .

Fig. 5.16 shows on the left the xb plane for the 15 A/mm² case in which the design ($x = 0.8$, $b = 0.436$) is displayed. This point represents the intersection of the 310 Nm and 30 A/mm curves. On the right of the same figure, you can see the result of the Demagnetization Analysis carried out at a current of 515 A. In fact, this design requires approximately 8000 Ampere-turns, and a number of N_s equal to 16 is chosen. This allows a base speed of around 5400 rpm to be achieved. Again, the volume of the magnet working beyond the linear section is very low (0.42%), making this design interesting for the purposes of the work.

A further decrease in current density does not lead to any advantage on demagnetization, as can be seen in Fig. 5.17.

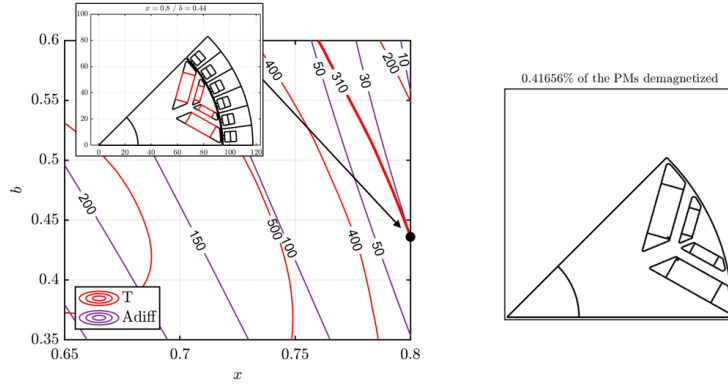


Figure 5.16: p4-q2 2V 15 A/mm²: xb plane design (on the left) and Demagnetization Analysis result (on the right).

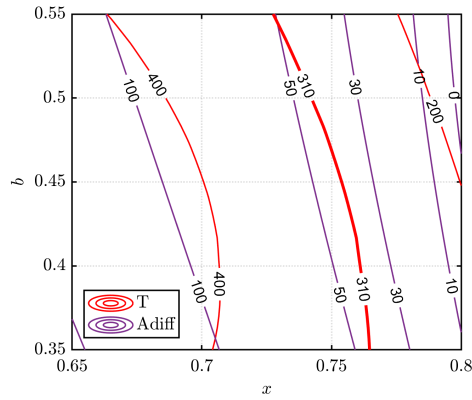


Figure 5.17: p4-q2 2V 10 A/mm² xb plane: Torque and A_{diff} .

5.3.3 Summary and Conclusions

Table 5.2 shows the main characteristics of the two possible solutions. With the 2V-shape geometry, unlike the 1V-shape, the torque target and acceptable demagnetization behavior can be achieved without exceeding the maximum value imposed on the active motor length.

The two designs shown in the table represent two valid solutions. The 8-pole case has a base speed closer to the desired target of 5500 rpm and lower demagnetization. For these reasons and for greater commonality with the benchmark motor, which is also an 8-pole motor, it is decided to continue the study with the 8-pole, 15 A/mm² motor.

Table 5.2: 2V-shape best designs.

		p3-q2	p4-q2
Current density	[A/mm ²]	20	15
Active length	[mm]	145	145
N_s		18	16
Torque	[Nm]	310	310
Base speed	[rpm]	4800	5400
Phase current	[A _{pk}]	470	515
Demag @ ph. current	[%]	0.48	0.42

5.3.4 Sensitivity Analysis

Starting from the identified design, a sensitivity analysis is made on the parameters in per unit introduced in Chapter 3.4. These parameters are:

- Tooth size factor k_t
- Stator yoke factor k_{ys}
- Rotor yoke factor k_{yr}

The xb planes presented up to now have been calculated with the standard values $k_t = 0.9$, $k_{ys} = 1.21$ and $k_{yr} = 1.1$. Fig. 5.19, 5.20 and 5.21 show the sensitivity analyses for the tooth size factor, the stator yoke factor and the rotor yoke factor, respectively.

It can be seen that while the change in k_t does not seem to bring any significant advantage, the situation is different for the k_{ys} and k_{yr} parameters. In fact, the value of $k_{ys} = 1.1$ allows the 310 Nm torque curve to exceed the 30 A/mm contour towards smaller values and approach the target base value curve of 5500 rpm. The behavior is similar when the value of k_{yr} goes from 1.1 to 1. For these reasons, the parameters used will be: $k_t = 0.9$, $k_{ys} = 1.1$ and $k_{yr} = 1$.

The new design (p4-q2-ideal) is shown in Fig. 5.18 and replaces the one (p4-q2-basic) shown in Fig. 5.16.

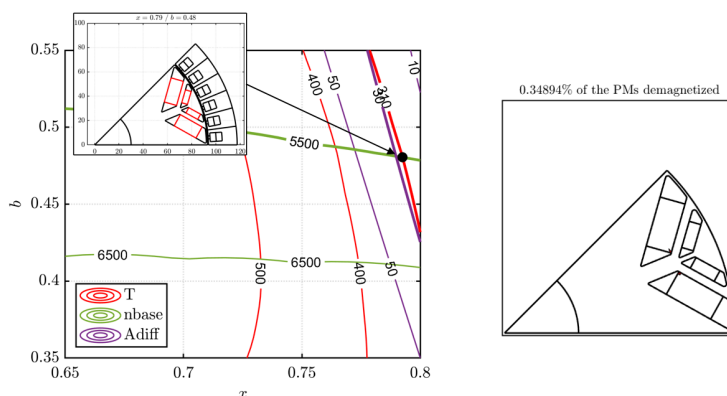


Figure 5.18: p4-q2 2V 15 A/mm² after sensitivity analysis: xb plane design (on the left) and Demagnetization Analysis result (on the right).

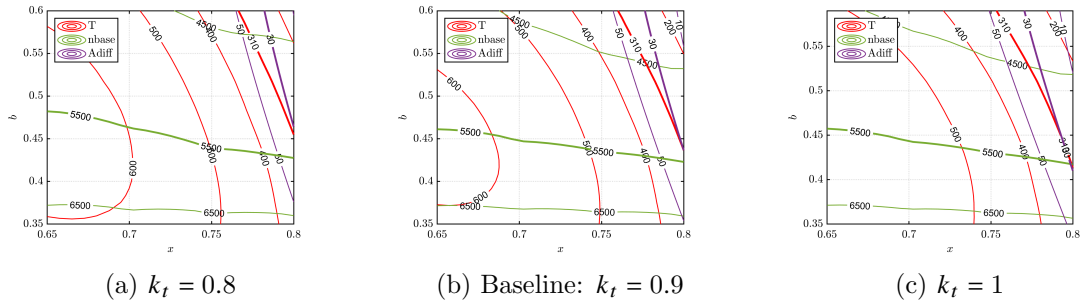


Figure 5.19: Tooth size factor sensitivity analysis.

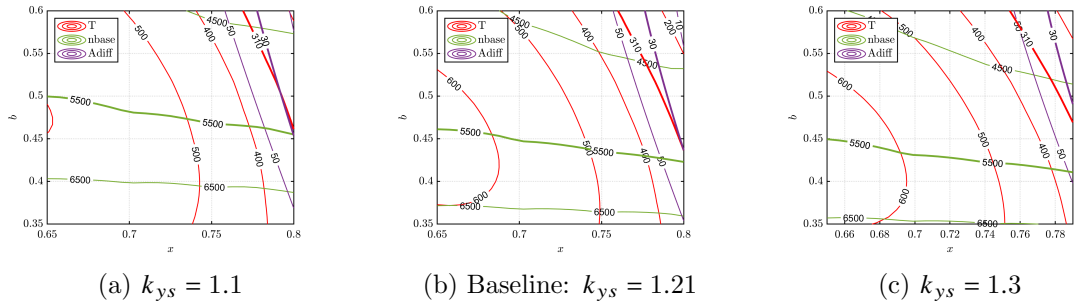


Figure 5.20: Stator yoke factor sensitivity analysis.

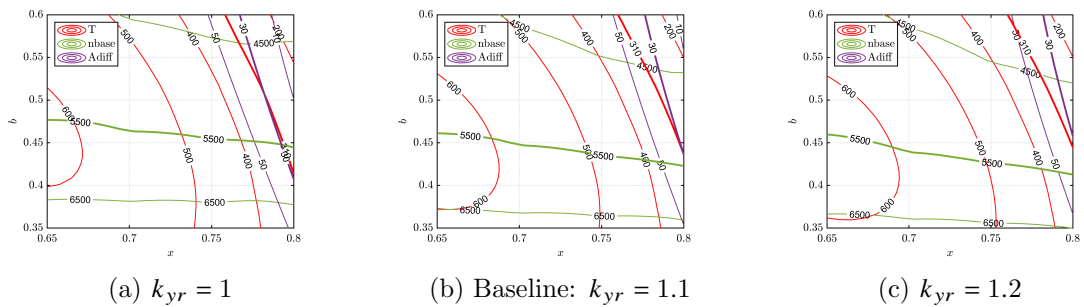


Figure 5.21: Rotor yoke factor sensitivity analysis.

On the left, in Fig. 5.18, we always find the design plane xb in which the torque curve at 310 Nm is always highlighted. Thanks to the new per unit parameters used, it can be seen that, unlike in the previous case, the target torque curve also lies at values less than 30 A/mm and also intercepts the desired base speed curve of 5500 rpm near the minimum value of A_{diff} . Again, the result of the demagnetization Analysis can be seen to the right of the figure. The percentage of the volume working beyond the limit of the linear section goes from 0.42% to 0.35%, despite the fact that the nominal current goes from 515 to 530 A. The improvement is most significant when looking at the resistance to demagnetization when going beyond the nominal current. For a current of 1.5 times the rated current, the demagnetization Analysis result goes from 76.6% (772 A for p4-q2-basic) to 58% (795 A for p4-q2-ideal).

5.4 Selected Design

The design shown in Fig. 5.18 has two critical aspects. The first concerns the rotor iron in the q-axis. SyR-e keeps the angles of the magnets and the position of the radial ribs fixed during the design and varies the thickness of the magnets by varying the parameter b . For the chosen plane point ($b = 0.48$), the thickness of the magnets is such that the outside of the largest barrier occupies almost all the available space. This results in a lack of iron in the q-axis, which weakens the motor both structurally and magnetically. The second critical point concerns flux weakening behavior. So much magnet volume results in a lot of flux that is difficult to counteract under flux weakening conditions with the little current provided to prevent demagnetization. This results in the impossibility of achieving the maximum speed target.

The solution adopted was to simply increase the radius of curvature of the tangential rib fillet of the inner barrier, going from the default value of 1 mm to 5 mm. Furthermore, the value of *PM filling factor [p.u.]* has been set to 0.8 for both barriers. This means that the length of the magnets will be 80% of the length they could occupy. In this way the amount of magnet used decreases and thus decreases the flux to be counteracted during weakening. A further advantage is given by the fact that decreasing the length of the magnet means moving the magnetic material away from the area where demagnetization is relevant, i.e. close

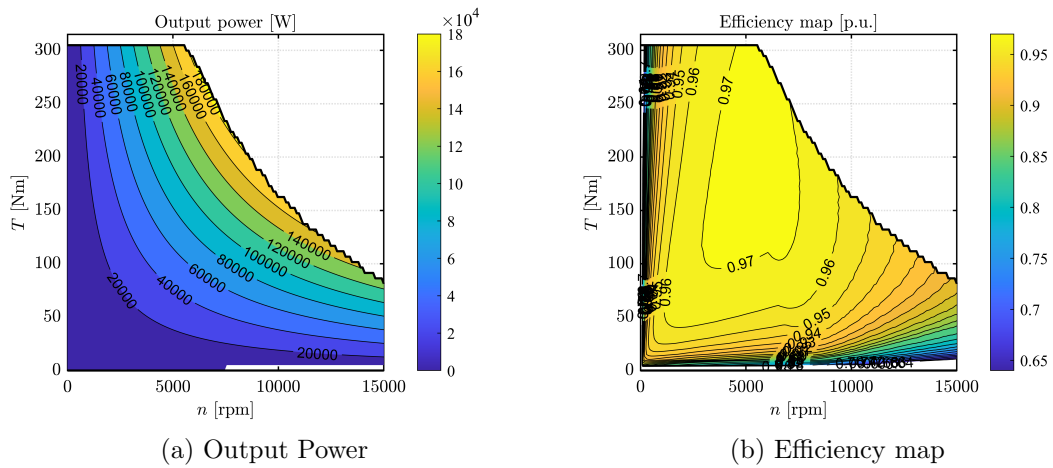


Figure 5.22: Characteristics of the p4-q2-mod motor.

to the airgap. Therefore, it will be possible to use a higher current to always reach the torque target, while maintaining the same demagnetization.

In this way the flux weakening behavior is certainly improved and from Fig. 5.22 it is possible to see that the maximum speed is reached even with more than good torque values. In Fig. 5.23 it is possible to see how the geometry of the cross section has changed.

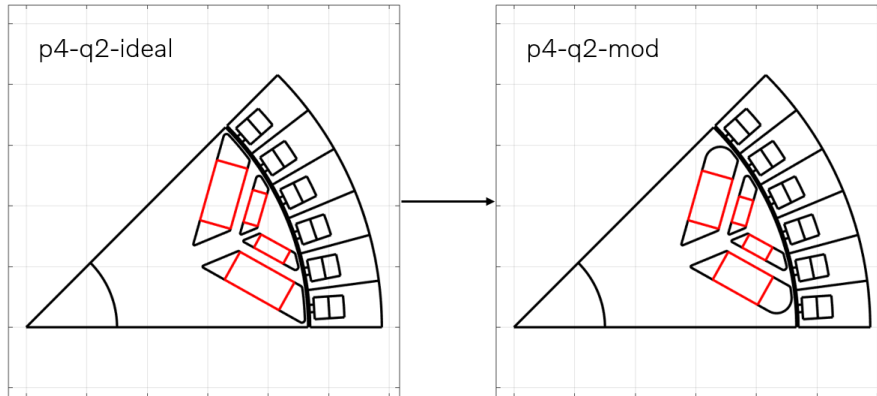


Figure 5.23: Cross section geometry: from p4-q2-ideal to p4-q2-mod.

In the Table 5.3 it is possible to find the summary of all the main characteristics of the motors seen: from the p4-q2-basic, passing through the p4-q2-ideal up to the p4-q2-mod. To achieve the same torque target, in the p4-q2-mod case, the current rating must rise to 555A to compensate for the lower PM flux. Despite

Table 5.3: p4-q2 motors recap.

		p4-q2-basic	p4-q2-ideal	p4-q2-mod
Current density	[A/mm ²]	15	15	15
Active length	[mm]	145	145	145
N _s		16	16	16
Torque	[Nm]	310	310	310
Base speed	[rpm]	5400	5500	5500
Phase current	[A _{pk}]	515	530	555
Demag @ ph. current	[%]	0.42	0.35	0.12
Demag @ 1.5 * ph. current	[%]	76.6	58	26.9

this, however, it is possible to see that the demagnetization at the rated current decreases passing from 2.63% to 0.9%. Similar and more evident behavior for the demagnetization at 1.5 times the rated current: from 58% to 26.9%. The p4-q2-mod motor is therefore the definitive design made using the SyR-e software.

6 Geometry Optimization using JMAG

JMAG [20] is a simulation software used for the development and design of electrical devices. It was originally released in 1983 as a tool to support the design of devices such as motors, actuators, circuit components, and antennas. JMAG allows a wide range of physical phenomena to be analyzed, including complicated geometries, different material properties, and heat. It also allows the simulation of supply circuits, thus being able to include power electronics in the simulations.



Figure 6.1: JMAG logo.

During this work, the JMAG software was used for two main purposes: to analyze the behavior of the machine previously designed with SyR-e when the linear approximation of the BH curve of the FeN magnets is replaced by the real non-linear characteristic and to carry out an optimization of the geometry. It is worth mentioning that SyR-e software also allows you to perform a design optimization with a MODE (Multi-Objective Differential Evolution) algorithm. This function is available in the *Optimization* tab of the main GUI. However, it was decided to use JMAG software for this purpose due to its possibility of using non-linear characteristics for the magnets. This makes it possible to take into account the real behavior of the magnets during optimization and also allows us to compare the results obtained with SyR-e and assess how correct the linear approximation used is. The model created for FeN PM takes into account both the non-linearity of the characteristic and the non-reversibility of demagnetization by allowing various points of the magnet to work on different recoil lines depending on the degree of demagnetization.

First, it was necessary to create the model capable of describing the FeN magnet

in JMAG and at the same time, the *demagnetization Ratio* was identified as the output provided by the software that allows us to evaluate demagnetization during operation and during the optimization process.

Then the geometry p4-q2-mod was recreated in *JMAG Designer* using the *JMAG Express* software, and the parameterization of the CAD file, automatically created by Express, was modified to facilitate optimization for our purposes.

Two different optimizations were made: the first one takes the results obtained with SyR-e as good and tries to optimize the geometry of the barriers only, slightly varying the variables describing their position and shape, in order to reach the targets while minimizing demagnetization. The second optimization, on the other hand, is more general, including among the optimizer's parameters also the rotor radius, and the stator geometry.

6.1 GEN2 Model and Demagnetization in JMAG

In order to create the model of the FeN PM in the JMAG software, taking into account the need to evaluate the phenomenon of irreversible demagnetization, a non-linear and irreversible model was used. In particular, the model [*Nonlinear (Irreversible/Thermal demagnetization/Demagnetising field) (Point Array)*] was used as [*Magnetic Property Type*] of the magnetic material. For this type of model, as can be seen from Fig. 6.2, deterioration (demagnetization) in magnet performance from increases in temperature and demagnetizing fields can be taken into account in the analysis.

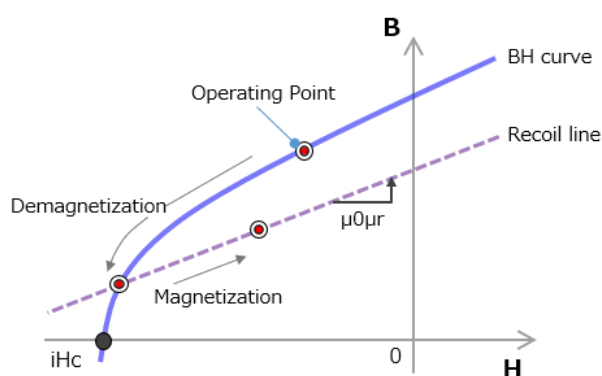


Figure 6.2: JMAG non-linear magnet model (*Point Array*).

When this type of model is chosen by the user for magnets, the following parameters must be specified:

- Temperature B-H Curve: BH curves at different temperatures;
- Temperature Recoil Table: slope of recoil lines at any temperature.

Specifically, BH curves describing the behavior of FeN magnets at different temperatures were entered here, while the slopes of the recoil lines at different temperatures were set all the same and all parallel to the linear section of the BH feature.

To evaluate demagnetization during simulations and during the optimization process, the *Demagnetization Ratio (Compared to undemagnetized state)* was used as *Output Physical Quantities*. This output returns the percentage of demagnetization, calculated using the expression (20), for each point of the magnet mesh. You can then decide how to summarize and display the results over time. Among the most suitable possibilities in the case of demagnetization, it is possible to choose to display the maximum value found, the average value over the area of the magnets, or the amount of area with a percentage demagnetization value above a certain threshold. In our case, since we want to accept that part of the magnet may be demagnetized during normal operation, we have chosen to use the amount of area exceeding a certain value as the output to evaluate the demagnetization phenomenon. During the optimization of the geometry, the same output was used as the objective function to be minimized.

$$Demagnetization\ Ratio\ (\%) = 100 \cdot \left(1 - \frac{B_r}{B_{r,und}(T)} \right) \quad (20)$$

Where:

- B_r is the residual flux density of the displayed step [T];
- $B_{r,und}$ is the residual flux density of the undemagnetized state [T];
- T is the element temperature of the displayed step [°C].

6.2 p4-q2-mod in JMAG

The p4-q2-mod geometry resulting from the design in SyR-e was reproduced in JMAG Designer using the JMAG Express tool. This software is a parameter-based motor design tool, similar to SyR-e, that allows you to quickly create a geometry, define materials and windings and quickly simulate some of the machine's dynamic characteristics directly in the Express tool. Alternatively, it is possible to export the geometry to JMAG Designer for deeper analysis. In this way, you will already have an initial parameterization of the geometry that can be a good starting point for any modifications and/or customization.

Once the geometry has been exported into JMAG Designer, the result will be as shown in Fig. 6.3 and can be compared with the geometry shown on the right in Fig. 5.23.

To simulate the dynamic characteristics of the machine, it is first necessary to perform a *Speed Priority*. This study allows different simulations to be carried out at varying current magnitude, angle, and speed. From the results, it then determines the characteristic of MTPA and MTPV and allows the optimum control to be defined. The calculation time is not very high because only the DC losses of the conductors are taken into account (by means of a resistance value entered by the user) and the eddy current losses in the PMs are not taken into account. From the Speed Priority it is then possible to extract certain operating points (current amplitude, current angle, rotor speed) to perform an *Accuracy Priority* study, in which all losses are included. Fig. 6.4 shows the result of the Accuracy Priority in terms of efficiency map and power torque curves, for a line voltage of 400 V and a current of 555 A.

Comparing the efficiency map calculated with JMAG and that calculated with SyR-e (Fig. 5.22), it can be seen that the two softwares give approximately the same results: a maximum torque of 305 Nm for SyR-e and 303 Nm for JMAG. The flux weakening behavior is slightly different, also due to a slight difference in the base speed calculated by the two tools: 5500 rpm for SyR-e and 5000 rpm for JMAG.

As far as demagnetization is concerned, analyses carried out with JMAG confirm for the p4-q2-mod design a good behavior against demagnetization. In Fig. 6.5 the contour plot of the demagnetization Ratio output can be seen, for the oper-

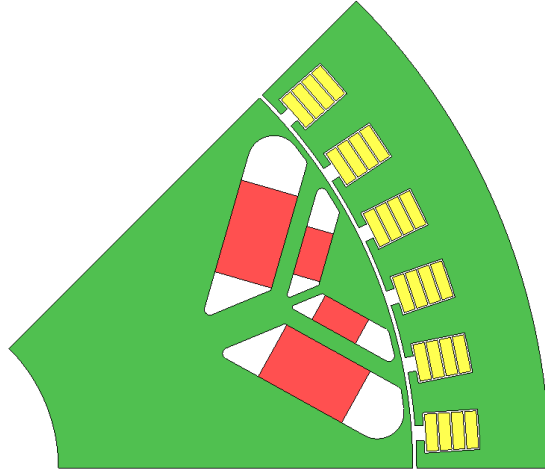
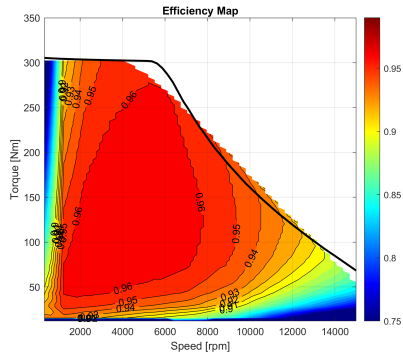
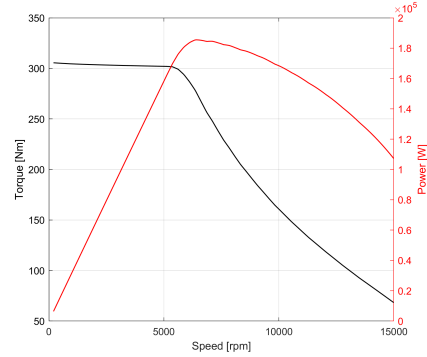


Figure 6.3: p4-q2-mod cross section in JMAG.

ating point at base speed and maximum torque (the scale of the color bar was limited to a value of 5% for graphical purposes). It can be seen that almost the entire magnet area shows values of less than 1%, with a maximum value recorded of 25%. Whereas, regarding the area above a certain threshold, two values are reported: 5.08 mm^2 is the magnet area that presents demagnetization above 1%, while 1.08 mm^2 is the magnet area that presents demagnetization above 5% out of a total magnet area of 443.58 mm^2 (the values in mm^2 refer to one pole only). The area parameters above the threshold of 1% and 5% will from now on be used for demagnetization analysis, also within the optimization processes.



(a) Efficiency Map



(b) Torque-Power

Figure 6.4: Characteristics of the p4-q2-mod motor on JMAG.

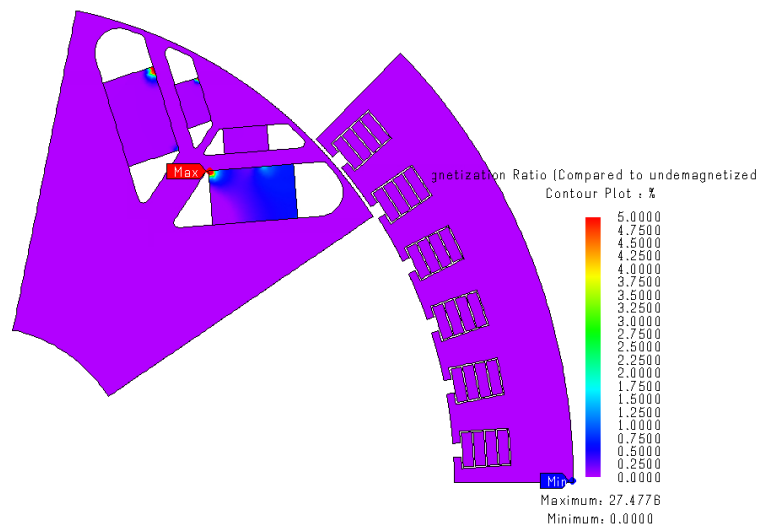


Figure 6.5: p4-q2-mod JMAG Demagnetization Ratio contour plot.

6.3 Geometry Optimization

The Multi-Objective Genetic Algorithm (MOGA) was used as optimization engine within the JMAG software. It uses genetic algorithms, which are inspired by the process of natural selection and evolution, to find a set of solutions that trade-off the conflicting objectives. Instead of finding a single optimal solution, MOGA generates a set of solutions, called *Pareto front*, that represent the best compromises between the objectives. The Pareto front provides decision makers with a range of alternatives to choose from, taking into account their own preferences and constraints. One of the benefits of MOGA is that it is flexible and can handle a wide range of objective functions, including linear and non-linear functions, continuous and discrete variables, and single and multi-objective problems. Moreover, it is able to search for solutions in high-dimensional and complex search spaces, where traditional optimization methods often fail.

When optimizing with a MOGA, it is necessary to specify the *Number of Generations* and *Population Size* values. Standard values used for these two variables are:

- Number of Generations = n^o parameters \cdot 10
- Population Size = n^o parameters + 1

where n^o parameters is the number of parameters you want to vary during optimization. For the population size, it is necessary to have a value at least higher than the number of parameters, so the recommended value is also the minimum acceptable. Increasing these values compared to the standard ones allows us to ensure that the result of the optimizer is a global minimum and not a local minimum. On the other hand, however, this leads to a significant increase in simulation time, so it is essential to find a good compromise.

In addition to the values of number of generations and population size, three other fundamental elements are required to realize a geometry optimization: a good parameterization of the geometry, the variation ranges of the parameters and the objective functions to be pursued during the optimization process. For the first, it is essential that the parameterization is already thought out knowing which geometric quantities are to be optimized, in order also to prevent the optimizer from converging towards unfeasible solutions. This also depends on the ranges of

variation of the variables and it is therefore important that the parameterization and margins are coordinated. As far as the objective functions are concerned, those best suited to the study under consideration can be used. For example, in our case it is essential to include demagnetization among the objective functions, trying to reach the targets by minimizing the volume of the demagnetized magnet.

In the following, the results of two different optimizations will be reported. The first, called p4-q2-mod optimization, represents a slight optimization of the design obtained with the SyR-e tool. In this optimization, all parameters describing the geometry of the rotor barriers will be included among the parameters to be optimized, while the outer rotor radius and everything describing the stator have been kept unchanged. In addition, the range of variation of the parameters considered will be kept narrow. In the second optimization, on the other hand, all the parameters describing the geometry will be included in the optimization, which is why it is called global optimization.

Both optimizations were carried out with the standard value for the number of generations, whereas the standard value for the population size was used for the first optimization, while for the largest optimization, the population size was significantly increased.

6.3.1 p4-q2-mod Optimization

Starting from the geometry designed with the SyR-e tool, an optimization of the barrier geometry is carried out in order to reach the torque target (310 Nm) while trying to minimize the demagnetization phenomenon and the active length of the motor, if possible. To this end, the objectives functions shown in Table 6.1, with their respective weights, have been defined. The weights determine the importance of each objective function in relation to the others present. In our case, the main objective function will be the average torque condition followed by the line voltage limitation and the functions that minimize the area of magnets with demagnetization greater than 5% and 1%, from now on abbreviated as A5% and A1%, respectively. Finally, we find the objective functions that aim to minimize the active length and maximum demagnetization point with much less weight than the others.

The optimization point is relative to the target base speed of 5500 rpm.

Table 6.1: Optimization objective functions.

Parameter	Type	Value	Weight
Torque	\geq	310	10
Line voltage	\leq	400	9
Area demag 5%	<i>Minimize</i>	—	8
Area demag 1%	<i>Minimize</i>	—	7
Length	<i>Minimize</i>	—	2
Max demag point %	<i>Minimize</i>	—	1

The parameters included in the optimizer include those defining the circuit power supply (current magnitude and angle) and all those describing the geometry of the barriers and their position in the rotor, shown in Fig. 6.6. The variation ranges of these parameters have been kept narrow in order to carry out an optimization of the geometry without totally modifying the SyR-e design. The parameter describing the width of the larger radial rib was also included, because it was structurally oversized by the SyR-e, while the smaller one that was slightly undersized (1.57 mm) was set at 2 mm. It was decided to include the larger rib in the optimizer because this was particularly decisive against demagnetization, while the smaller rib was not. Having very large ribs results in a higher leakage flux and thus a lower electromagnetic torque, so it was decided to structurally check the minimum value and include them in the optimization process.

The result of the optimization will be many different geometries and the results of all simulations performed on each geometry. To visualize the results and choose the preferred geometry, it is possible to print out two-variable plots to see how the various cases are placed as the two chosen variables change. In Fig. 6.7 you can see the Torque-A1% plot where each of the squares represents a different geometry. In producing this plot, all constraints have been applied so each geometry meets the torque and voltage requirements. The zoomed-in window beside shows the identification numbers of the four best cases next to the respective squares, and the respective geometries are shown in Fig. 6.8. As can be seen, these geometries are very similar and the differences are almost imperceptible when looking at them. The logic with which the geometries were selected is to minimize demagnetization

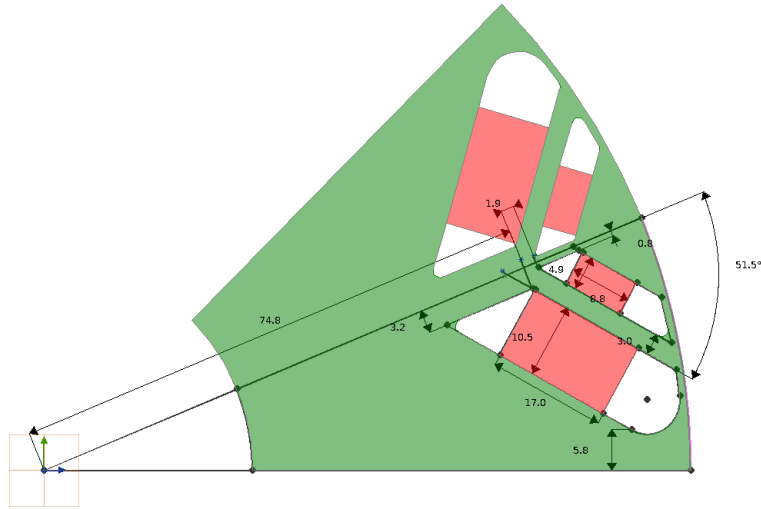


Figure 6.6: p4-q2-mod optimization parameters.

as much as possible by "minimizing" torque. In fact, "minimizing" the average torque, while still guaranteeing a value greater than 310 Nm, certainly means minimizing the length.

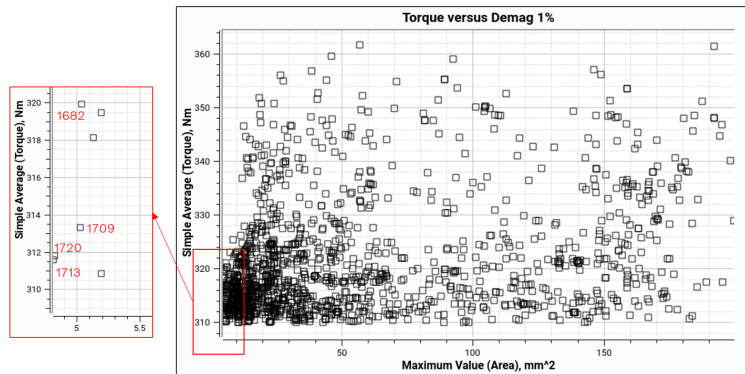


Figure 6.7: Optimization results: Torque-A1%.

The same thing was done for the Torque-A5% plot to see the relationship between the best geometries of the two objective functions. Fig. 6.9 and Fig. 6.10 show the plot and the best four geometries, respectively, while Table 6.2 shows all the main characteristics for the eight geometries considered.

From the values shown in the table, it can be seen immediately that all eight

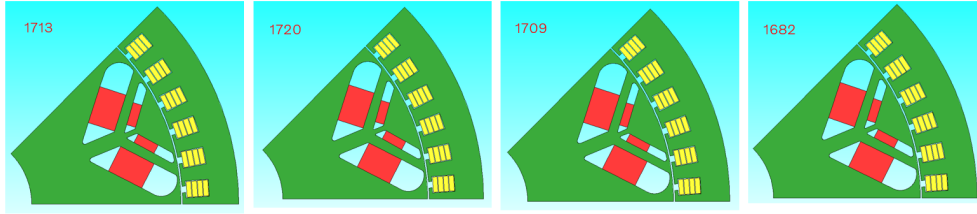


Figure 6.8: Optimization results: Torque-A1% best cases.

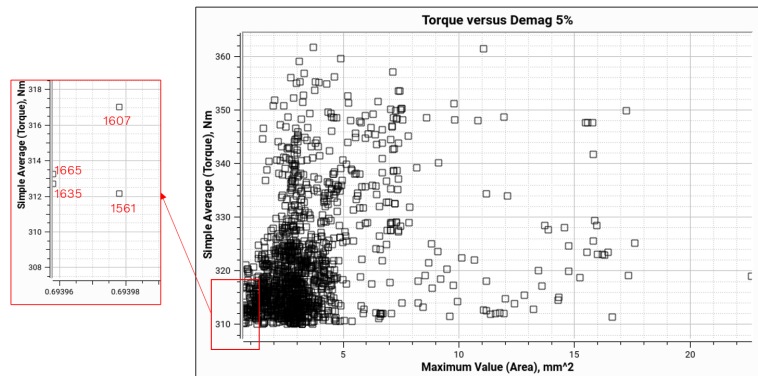


Figure 6.9: Optimization results: Torque-A5%.

geometries have an active length of approximately 135 mm, which represents an improvement of approximately 10 mm from the 145 mm long SyR-e design. Furthermore, despite the shorter length, there is also an improvement with regard to demagnetization.

Looking at the column values of A1% and A5%, it can be seen that it is more convenient to choose the design based on the values of A1%, so the design with the lowest value of A1% was chosen, i.e. case 1713. The cross-section geometry of selected case can be seen in Fig. 6.11(a), while Fig. 6.11(b) shows the 1713 geometry overlapping the p4-q2-mod geometry.

Interestingly, the result of the optimization led to a fairly large radial rib (6.29 mm), close to the value used in the SyR-e design (6.47 mm), preferring to preserve demagnetization against torque.

As for the p4-q2-mod design, to evaluate the dynamic characteristics of the 1713 design, a Speed Priority study was first carried out, followed by an Accuracy Priority study. Fig. 6.12 shows the efficiency map and the torque and power limit

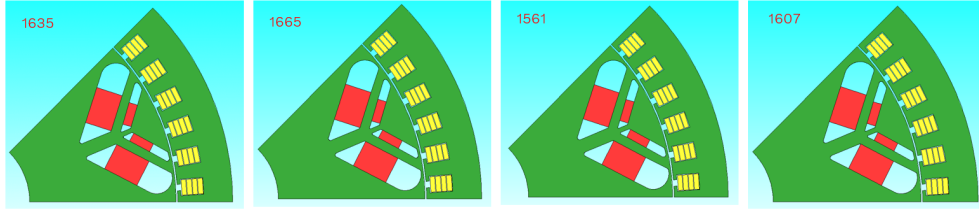
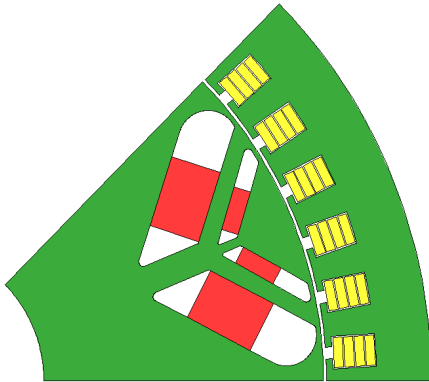


Figure 6.10: Optimization results: Torque-A5% best cases.

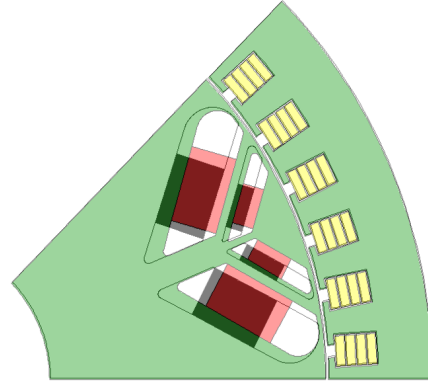
Table 6.2: Optimization results best cases.

Case	Torque [Nm]	V_{max} [V]	Max de- mag point	A1% [mm ²]	A5% [mm ²]	Length [mm]	Current [A _{pk}]
1713	311	394	24%	4.81	0.84	135	666
1720	311	394	24%	4.82	0.84	135	666
1709	313	395	22%	5.1	1.10	135	666
1682	319	398	22%	5.1	0.88	138	674
1635	312	396	24%	5.78	0.7	135	666
1665	313	396	24%	5.77	0.7	135	666
1561	312	395	25%	5.65	0.7	135	666
1607	317	400	25%	5.89	0.7	137	666

curves. Compared to the previous case, this design has a better efficiency map, visible for example by a larger efficiency zone of more than 97%. This is despite the fact that the 1713 case has a higher do current (666 A) than the p4-q2-mod case (555 A) and consequently higher Joule losses. It is important to emphasize that the optimization process is driven by the goal of lower demagnetization and that the efficiency has not been optimized, so this result is entirely fortuitous. Another improvement is visible on the power curve, which exhibits flatter behavior under flux weakening conditions. The maximum power is approximately 220 kW, which is higher than the 180 kW value for the p4-q2-mod design. This is due to a higher torque value of 310 kW and a higher base speed value slightly above the target value of 5500 rpm.

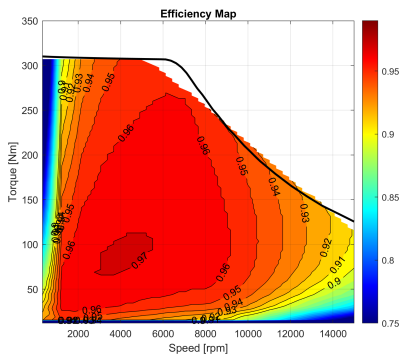


(a) 1713 case

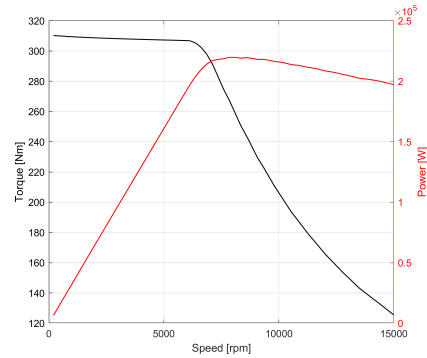


(b) 1713 over p4-q2-mod

Figure 6.11: SyR-e optimization: chosen design.



(a) Efficiency Map



(b) Torque-Power

Figure 6.12: Characteristics of the 1713 motor.

6.3.2 Global Optimization

For global optimization, the parameters to be entered in the optimizer include, in addition to those considered in the previous optimization, the radius of the outer rotor and all the parameters describing the stator (Fig. 6.13). The stator inner radius is determined by the rotor outer radius and the airgap value (always kept constant and equal to 0.7 mm), tooth width and the height of the back iron are varied and the latter determines the slot height. The winding scheme has been kept unchanged, only modifying the pin dimensions to adapt them, case by case, to the slot dimensions.

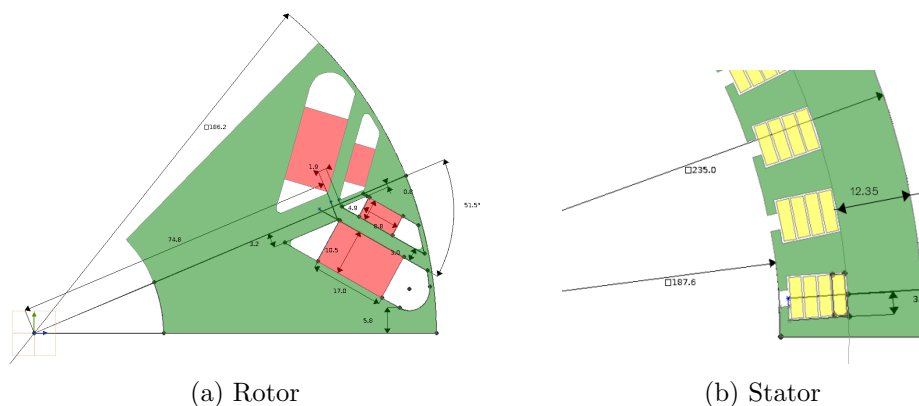


Figure 6.13: Global optimization parameters.

In addition to the increase in the parameters involved, both the variation ranges of each parameter and the population size value were increased. The latter was increased from the standard minimum value (number of parameters plus one) to three times the number of parameters. This will make it possible to analyze a larger solution space and ensure that we converge towards a global minimum.

The objective functions have not been changed from those presented for the previous optimization (Table 6.1).

To visualize the results and select the best geometry, the same procedure presented for the previous optimization is followed. The Torque-A1% plot and cross section geometries of the best cases are shown in Fig. 6.14 and Fig. 6.15, respectively. Again, the Torque-A5% plot and best case geometries are shown in Fig. 6.16 and Fig. 6.17, for completeness. In fact, as seen above, the behavior of A1% and A5% indicate that it is most convenient to select the best case according to the

value of A1%. This is again confirmed and can be seen in Table 6.3, where the main characteristics of the selected best geometries are also shown. Among the best designs, case 7328 is selected as it has the lowest maximum demagnetization value but also the best compromise between A1% and A5%.

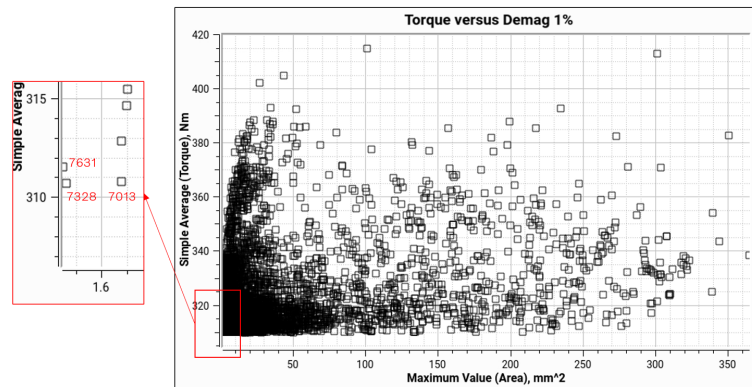


Figure 6.14: Optimization results: Torque-A1%.

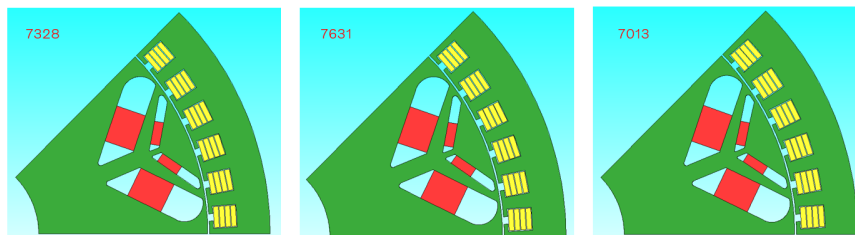


Figure 6.15: Optimization results: Torque-A1% best cases.

From the data in the table, it can be seen that the demagnetization values are much improved compared to the previous optimization. The maximum demagnetization point goes from 24% for design 1713 to 5.9% for design 7328. Area values with demagnetization greater than 1% (from 4.81 mm² to 1.53 mm²) and 5% (from 0.84 mm² to 0.13 mm²) also improve, despite an increase in phase current (from 666 A to 749 A). The torque and voltage targets are met, and the active length is almost unchanged (135 mm in case 1713 and 136 mm in case 7328).

A data not present in the table, but important to report, is the current density of 18.1 A_{rms}/mm^2 for case 7328. This value is higher than that of case 1713 (17.1

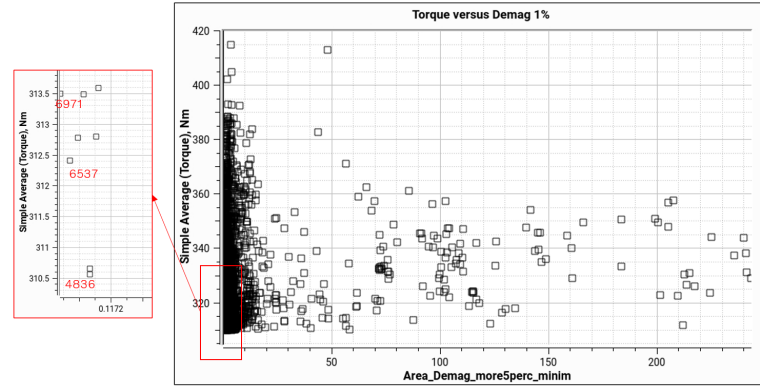


Figure 6.16: Optimization results: Torque-A1%.

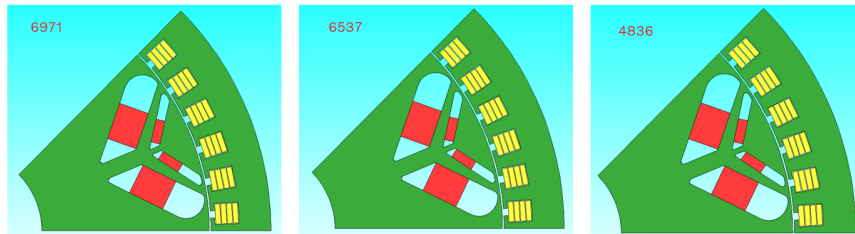


Figure 6.17: Optimization results: Torque-A5% best cases.

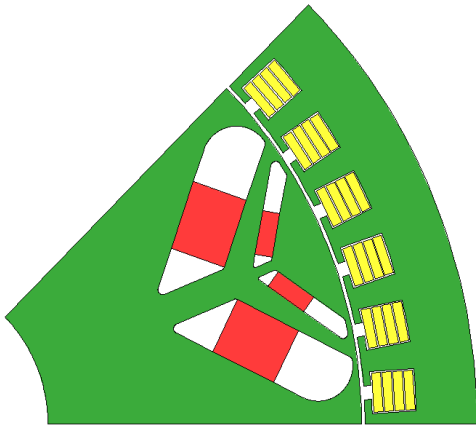
A_{rms}/mm^2) and is due to the increase in phase current despite a slight increase in the conductor section.

Fig. 6.18 shows the geometry of the cross section for case 7328 and the same geometry overlaid on the result of the previous optimization. It can be seen that the stator remains virtually unchanged: the rotor outer radius (and consequently the stator inner radius) are approximately 1 mm larger than those obtained during the design performed with SyR-e, as are the slots, which in the case of 7328 are slightly wider and have essentially the same height. This gives strong confirmation of the design carried out using SyR-e and the analytical theory presented.

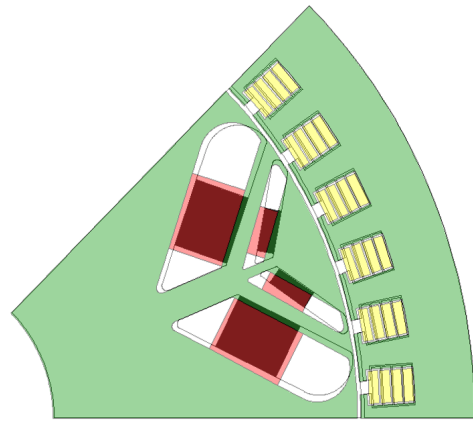
In Fig. 6.19, the efficiency map and the torque and power limit curves are shown as before. The best demagnetization behavior is achieved at the expense of a worse efficiency map with a maximum value below 97%. This is also due to an increase in phase current and a consequent increase in DC and AC Joule losses. The power curve shows a maximum torque of about 225 kW with practically constant behavior under flux weakening conditions.

Table 6.3: Global optimization results best cases.

Case	Torque [Nm]	V_{max} [V]	Max de- mag point	A1% [mm ²]	A5% [mm ²]	Length [mm]	Current [A _{pk}]
7631	311	400	6.4%	1.52	0.23	136	749
7328	310	399	5.9%	1.53	0.13	136	749
7013	310	394	8.8%	1.64	0.13	136	754
6971	313	378	12%	2.58	0.12	132	749
6537	312	377	10.5%	2.45	0.12	133	749
4836	310	386	9.9%	2.33	0.12	133	750

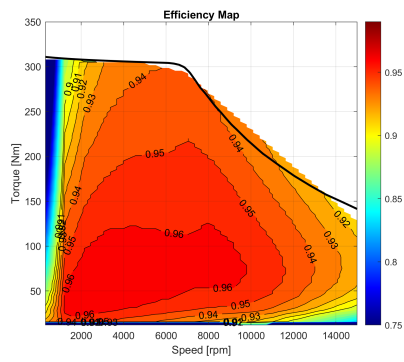


(a) 7328 case

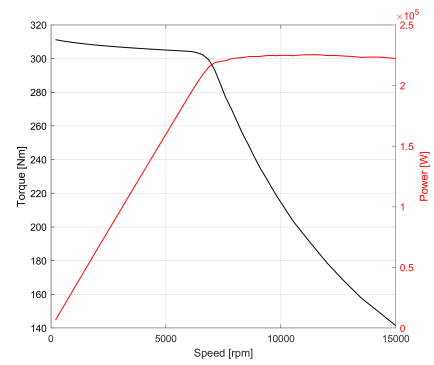


(b) 7328 over 1713

Figure 6.18: Global Optimization: chosen design.



(a) Efficiency Map



(b) Torque-Power

Figure 6.19: Characteristics of the 7823 motor.

7 Final Comparisons

This chapter reports the comparison between all the designs presented during this thesis work, whose geometries are shown in Fig. 7.1. The reference motor with RE magnet will then be compared with the design realized with SyR-e tool and the two designs obtained from the optimization process. For the design carried out using SyR-e, the characteristics calculated using the JMAG software will be reported since these take into account the real non-linear characteristic of FeN magnets.

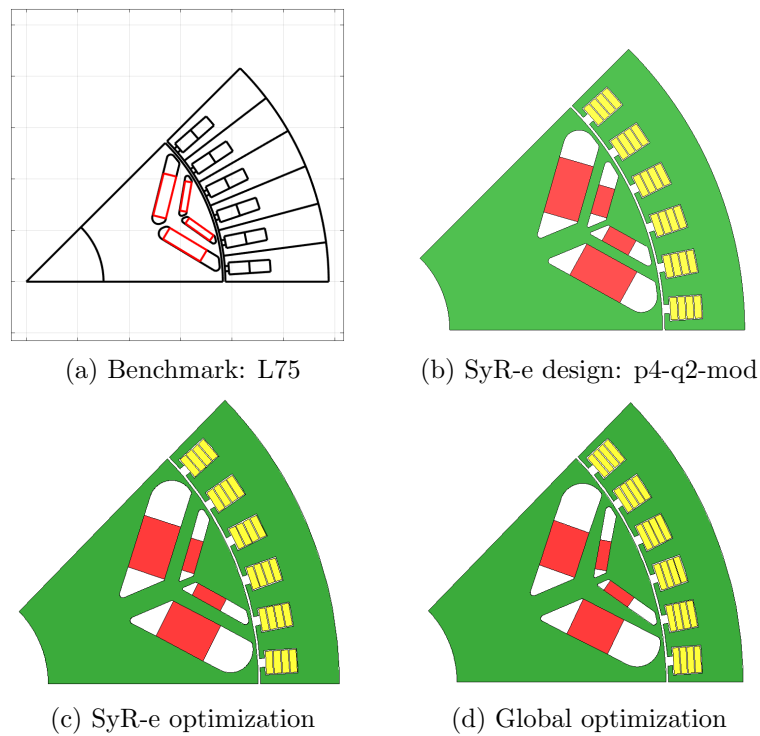


Figure 7.1: Comparison of the cross-section geometry of the designs.

The comparison focuses on the following items:

- machine performance:
 - torque/power - speed characteristics;
 - torque ripple;
 - efficiency;

- demagnetization;
- environmental impact.

Table 7.1: Final comparison.

	Torque [Nm]	V_{max} [V]	Max de- mag point	A1% [mm ²]	A5% [mm ²]	Length [mm]	Current [A _{pk}]
Benchmark	304	400	0%	0	0	75	717
SyR-e design	303	460	25%	5.08	1.08	145	555
SyR-e opt	311	394	24%	4.81	0.84	135	666
Global opt	310	399	5.9%	1.53	0.13	136	749

7.1 Machine Performance

7.1.1 Torque/Power - Speed Characteristics

Fig. 7.2 shows the torque-speed (left) and power-speed (right) limit curves for the four motors considered. From the torque graphs, it can be seen that the motors with SyR-e optimization and global optimization achieve the target torque of 310 Nm when all losses are taken into account, unlike the reference motor and the SyR-e design, which have maximum torques below 305 Nm. In addition, the first two designs have a slightly higher base speed than the second two designs. This translates into higher maximum power as is visible from the power-speed plot.

It is possible to see an improvement in power under flux weakening conditions. Moving from the SyR-e to SyR-e optimized design and ending with the global optimization design the power tends to decrease less and in the case of the global optimization motor it is almost constant.

7.1.2 Torque Ripple

In Fig. 7.3 it is possible to visualize how the torque ripple varies on the torque-speed map for the four designs under consideration. The values are given in p.u., i.e. the peak-to-peak torque ripple divided by the average torque value. The

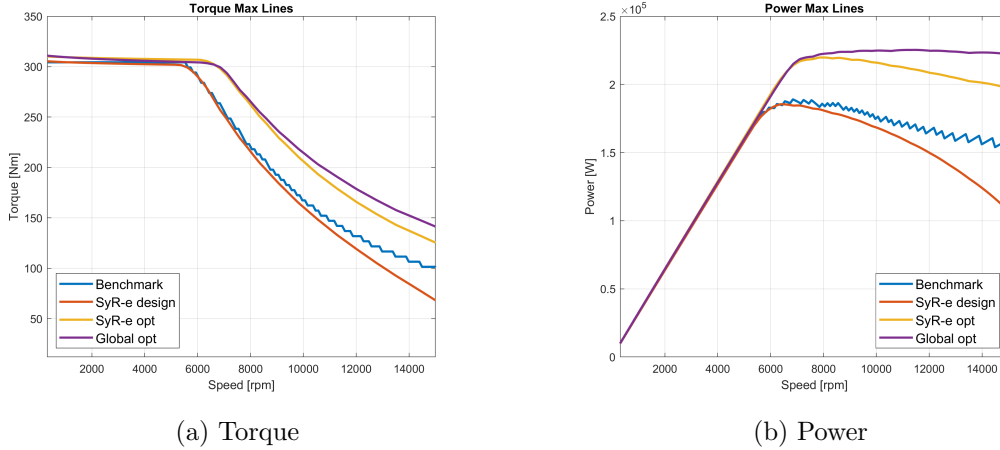


Figure 7.2: Comparison of torque and power limit curves.

coloring was kept different to highlight the different origin of the data. The torque ripple of the benchmark is in fact calculated by SyR-e while the other three are derived from data calculated by JMAG.

Optimizations were mainly focused on the geometry of the barriers, varying their position and shape. This inevitably affects the torque ripple, since the harmonics of the flux density at the airgap are affected. From the graphs shown, it can be seen that the benchmark motor presents the best behavior with a wide zone with values below 0.2 p.u. As for the motors with RE-free PMs, on the other hand, it is possible to see an improvement in torque ripple during the optimization process, with the global optimization design presenting the best behavior of the three with the widest zone at 0.3 p.u. and values below 0.2 p.u. for torque values near the torque limit.

However, it should be noted that, as with efficiency, torque ripple was never included among the objective functions to be minimized during optimization, so this improvement should be considered fortuitous.

7.1.3 Efficiency

Fig. 7.4 shows the efficiency maps of the four designs under investigation. The benchmark motor efficiency map was calculated using SyR-e software, while the other three are calculated by JMAG software and then plotted using Matlab. Again, the coloring was kept different to highlight this different origin of the data.

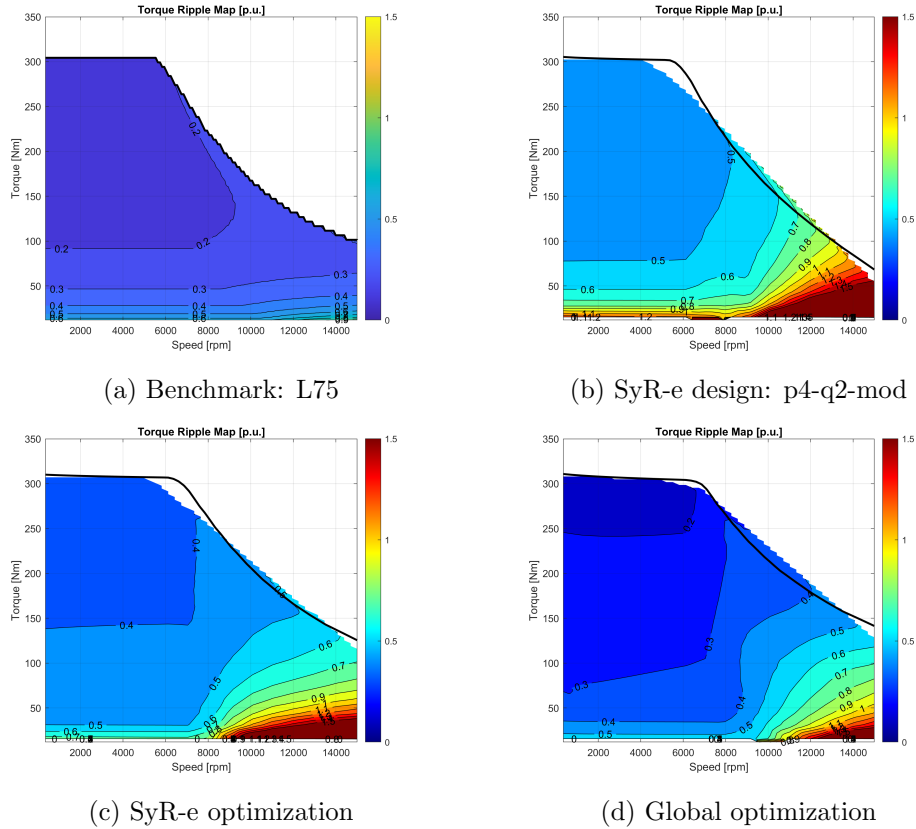


Figure 7.3: Comparison of torque ripple.

In all efficiency maps, all losses were considered: DC losses, AC losses, and iron losses.

Regarding DC losses, the two softwares differ in the calculation of conductor length. In fact, while SyR-e estimates the length of the end-windings by considering them in the calculation of the conductor resistance and thus in the losses, JMAG considers only the active length of the conductors and does not consider the losses of the end-windings in any way. To take into account the length of the end-windings also in the models studied with the JMAG software, the estimation made by SyR-e for the SyR-e design was used. The total length of the windings turns out to be about 1.7 times the length of the active parts only, so a coefficient of 1.7 was used in the calculation of the Joule losses estimated by JMAG. The same coefficient was also used for the global optimization design because the winding and stator dimensions are approximately unchanged.

On the other hand, regarding the calculation of iron losses, usually, a multiplicative coefficient is applied to the loss estimate made by the software, and the same value of 1.5 was used for both software.

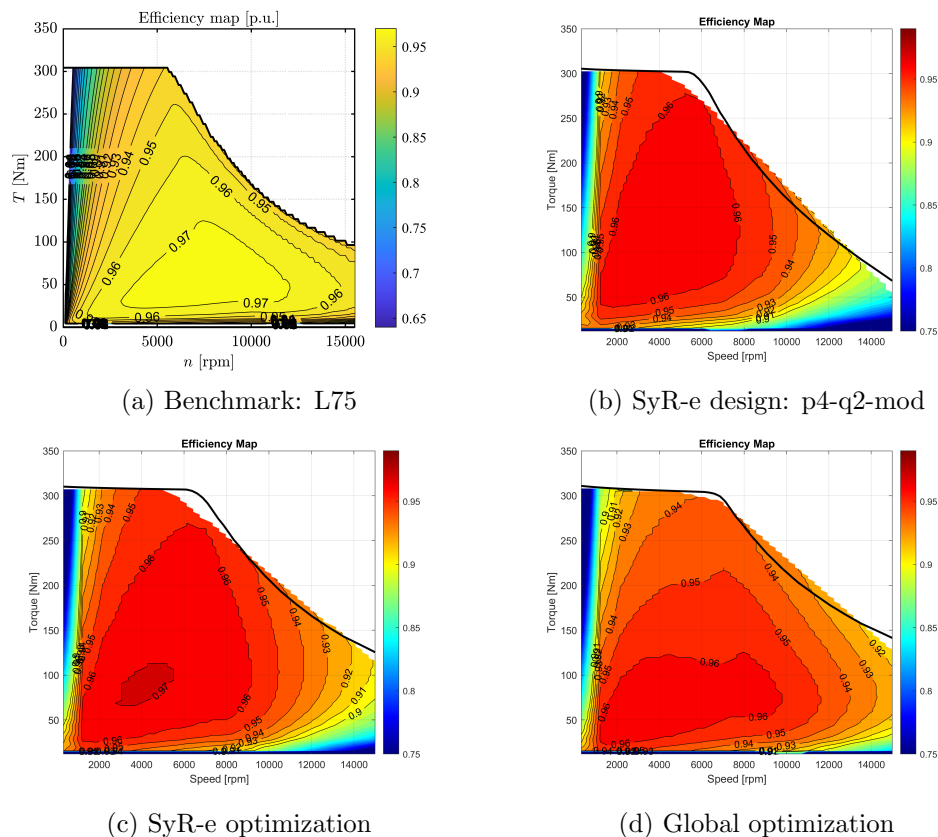


Figure 7.4: Comparison of efficiency maps.

The four maps have maximum values between 96% and 97%. To better compare the performance, the efficiency values at two different vehicle speeds, 80 - 120 km/h, for three different torque values, 20 - 30 - 40 Nm, are shown in Table 7.2. The speed and torque values are the same as those already used for the benchmark motor design.

For the SyR-e design, values calculated from the SyR-e and JMAG efficiency maps are shown as a comparison in Fig. 7.5. In comparing these two maps, it must be remembered that the two software use a different model to describe the magnets. Despite this, it can be seen that the JMAG software estimates higher losses than SyR-e as can be seen from the lower efficiency values in the right plot.

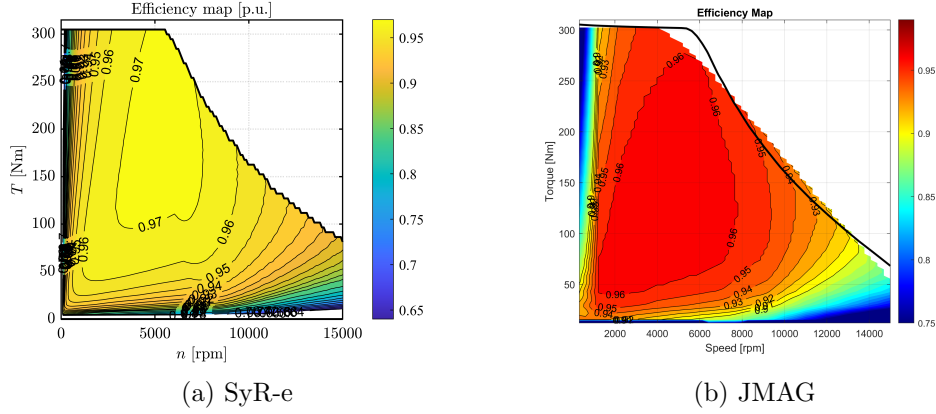


Figure 7.5: Comparison of SyR-e design efficiency maps calculated with the two software.

From the values shown in the table, it can be seen that the reference motor has higher efficiencies at all points of interest; the lower volumes of copper and iron inevitably lead to lower losses. The global optimization design is the motor with RE-free magnets that comes closest to the benchmark. Although it has lower efficiencies at high torque values, when looking at the points of interest it has the highest efficiencies values.

Table 7.2: Efficiency points comparison.

		Bench- mark	SyR-e design (SyR-e)	SyR-e design (JMAG)	SyR-e Opt	Global Opt
80 km/h	20 Nm	0.968	0.918	0.913	0.936	0.944
	30 Nm	0.973	0.939	0.938	0.952	0.955
	40 Nm	0.974	0.952	0.947	0.958	0.959
120 km/h	20 Nm	0.964	0.891	0.876	0.911	0.933
	30 Nm	0.971	0.919	0.908	0.937	0.948
	40 Nm	0.974	0.932	0.923	0.945	0.954

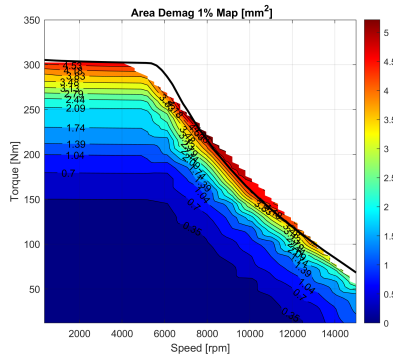
7.2 Demagnetization

In the analyses previously shown, we tried to assess demagnetization in the worst case, considering the current all against the magnets as done during the study with the SyR-e software, or at the point with base speed and maximum torque, as done during the geometry optimization process with the JMAG software.

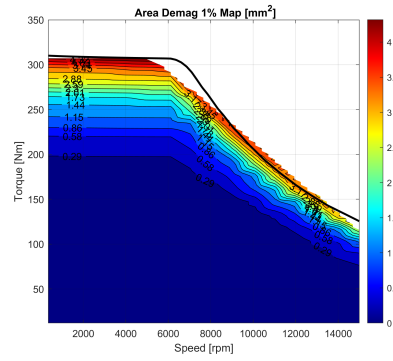
To better evaluate the demagnetization phenomenon through the torque-speed map, it is interesting to observe the graphs shown in Fig. 7.6. The plot for the benchmark motor is not shown because, as well known, NdFeB magnets do not incur any demagnetization under normal operating conditions and temperatures. However, when FeN magnets are used instead of RE NdFeB magnets, this is no longer valid. As we have seen throughout the thesis work, it is impossible to guarantee a demagnetization current that is much higher than the normal operating current, and therefore it is necessary to accept that a small area of the magnet does not work in the linear section of the characteristic.

Fig. 7.6 shows the area values exceeding the demagnetization ratio of 1% on the torque-speed map. The values shown in the plots always refer to a single pole. It can be seen that, in addition to the improvement in demagnetization at the point with base speed and maximum torque already shown in the optimization results, the optimization process leads to an overall improvement in demagnetization over the entire torque-speed map. In fact, while SyR-e design and optimized SyR-e present values of approximately 5 mm^2 around base speed and maximum torque, for the global optimization design these do not exceed 3 mm^2 , reaching higher values only under flux weakening conditions. It is also possible to see how, when switching from the SyR-e design to the global optimization design, the dark blue area representing the area of the map where demagnetization is practically absent increases.

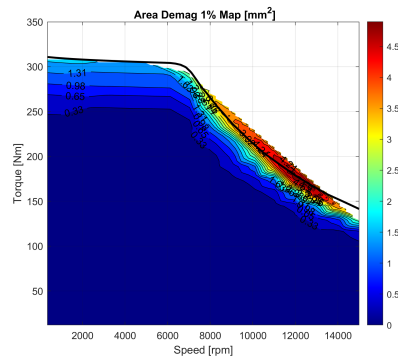
When displaying these values, it is important to make a clarification. During the optimization process, the parameters to be optimized also included those describing the power supply, i.e. current magnitude and angle, and both obviously affect demagnetization and torque. However, when plotting efficiency maps, a supply current on the MTPA characteristic is considered and it is not necessarily true that the angle that can provide the highest torque is the same as the angle that can provide the lowest demagnetization. In fact, it has been seen that in both



(a) SyR-e design: p4-q2-mod



(b) SyR-e optimization



(c) Global optimization

Figure 7.6: Comparison of $A1\%$ values on full torque-speed maps.

optimizer results, the optimum angle at base speed and maximum torque does not exactly match the angle at the same point on the MTPA. However, by comparing the $A1\%$ values given in the tables in the previous chapter, referring to the point at base speed and maximum torque, with those visible in the graphs at the same point, it is possible to see that in these cases the values are very similar.

7.3 Materials and Environmental Impact

One of the main issues driving the search for alternatives to RE PMs is the environmental damage caused by the extraction and separation process of the various REEs. This thesis work was guided by the goal of high environmental sustainability, as this is one of the main strengths of FeN RE-free PMs.

To compare the four designs from this perspective, the *Environmental Priority Strategies* (EPS) and *Climate Impact* values will be used. These two values take into consideration the environmental price to be paid for the production of the required materials. The EPS value is derived from the environmental impact of each type of material evaluated in Environmental Load Units (ELU) per kilogram (ELU/kg), multiplied by the mass of each material used. The ELU will therefore be the unit of measurement for EPS. The unit of measurement for climate impact, on the other hand, is kilogram of CO₂ equivalent (kgCO₂eq).

Table 7.3 shows at the top a comparison of the weights of the main materials in the four designs. The benchmark motor is the lightest of the four (23.6 kg) because it has an active length of only 75 mm. Designs using FeN PMs are forced to have greater lengths and consequently greater weights. This is due to the lower current density that can be used to avoid demagnetization (18.1 A_{rms}/mm² of the global optimization design vs. 33.7 A_{rms}/mm² used for the benchmark motor). The heaviest design is the SyR-e design because it has a longer active length (145 mm) than all the others.

In addition to the data on material weights, the EPS and climate impact values calculated for the magnets alone and for the entire motor are reported. In the case of EPS, the data including both motor and inverter in the calculation is also given. The projects considered have a different rated phase current and this data allows us to take into account the fact that motors with higher currents require larger inverters and consequently with higher ELU values.

Values are shown in p.u. of those calculated for the benchmark in order to highlight the differences more clearly.

Looking at the ELU and kgCO₂eq values for the magnets alone, it is possible to see the incredible advantage that the FeN PMs have over the RE PMs used for the benchmark motor (N42UH). Even though the benchmark is the design with the smallest amount of magnets, these result in much higher ELU and kgCO₂eq

Table 7.3: Materials and environmental impact data comparison.

		Bench- mark	SyR-e design	SyR-e opt	Global opt
Iron	[kg]	19.05	34.33	30.95	31.35
Copper	[kg]	3.45	5.84	5.43	5.81
Magnet	[kg]	1.1	3.6	3.34	2.9
Total motor mass	[kg]	23.6	43.8	39.7	40.1
Magnets climate impact	[p.u.]	1	0.283	0.262	0.226
Motor climate impact	[p.u.]	1	1.318	1.198	1.214
Magnets EPS	[p.u.]	1	0.012	0.011	0.010
Motor EPS	[p.u.]	1	1.371	1.272	1.356
Motor+Inverter EPS	[p.u.]	1	0.949	1.020	1.111

values than the magnets of the FeN PMs designs, which have around three times the PM amount.

However, when the entire motor is considered, it can be seen that the benchmark motor has lower values for both EPS and climate impact. The shorter active length of the benchmark motor allows both the amount of iron and copper required to be reduced. In designs using FeN PMs, the increase in EPS and climate impact due to the increased weight of these materials is greater than the decrease in the same values due to the use of RE-free PMs. In particular, copper has very high ELU/kg and kgCO₂eq/kg values, so an increase of a few kilograms of copper leads to very large increases in both EPS and climate impact.

When the inverter is also considered in the EPS calculation, it can be seen that the benchmark motor no longer has the lowest value. The higher phase current (717 A) results in higher ELU values for the inverter than for the SyR-e (555 A) and optimized SyR-e (666 A) designs. The highest EPS value is that of the global optimization design, as this design has an active length of 136 mm and a phase current greater than that of the benchmark (749 A).

8 Conclusions and Future Developments

8.1 Conclusions

The aim of this thesis work was to evaluate the pros and cons of Iron Nitride magnets and to define the design strategy when these magnets are used for motors that require automotive traction characteristics.

From the analysis of the BH characteristics describing the magnetic behavior of these magnets, it was found that the critical aspects are: high remanence values, low-temperature coefficients that allow stable performance at varying operating temperatures, lower coercivity, and the presence of a knee in the second quadrant that make the magnets not very resistant to demagnetization.

The remanence values are higher than some commercially available RE NdFeB magnets and, consequently, much higher than those presented by hard ferrites, typically used as RE-free solutions. On the other hand, they have coercivity values comparable to those of hard ferrites and even lower linear sections due to the presence of the knee. Such narrow linear sections of the BH characteristic in the second quadrant require special attention during machine design to ensure that there is no partial, or total, demagnetization during normal operation.

In order to compare the performance of a design using RE-free magnets, a benchmark motor was designed in a very compact solution that particularly exploits the advantages of NdFeB magnets, allowing the creation of a motor capable of reaching the required targets with reduced material requirements.

For the design of the motor with FeN RE-free magnets, the SyR-e tool and its syrmDesign functionality were used. Since the main problem of FeN magnets is given by their poor resistance to demagnetization and syrmDesign did not allow to include this requirement, the functionality was enriched with the possibility of estimating the maximum electrical load tolerable by the magnets. It soon became clear that it would not be possible to design a motor capable of having a demagnetizing current greater than the rated current of the motor. Therefore, it was decided to search for the best design that could achieve the required goals while minimizing the phenomenon of demagnetization.

The 1V-shape design was found to be unable to achieve the torque and maximum active length target without leading to almost complete demagnetization of

the magnets. By using a 2V-shape geometry, however, it was possible to design a design capable of reaching the required targets with acceptable demagnetization. Since the current that can be used is equal to the demagnetization current, all these designs require longer active lengths to achieve the required torque target. In particular, the final design has an active length of 145 mm, which also corresponds to the value that has been settled as the maximum length target.

We then moved on to optimize the geometry through the use of JMAG software capable of evaluating the true behavior of the magnets due to the possibility of including non-linear BH characteristics. The objectives pursued during the optimizations were the minimization of the demagnetization phenomenon and the length of the active motor.

In conclusion, a comparison of the four presented designs is reported: the benchmark motor, the design carried out in SyR-e, and the results of two different geometric optimizations. The emphasis of the comparison is on the machine performance, behavior against demagnetization, and environmental impact of the four presented designs.

The comparison shows that it is possible to design a motor with the torque and power characteristics required for automotive traction with acceptable values of active length while keeping the demagnetization phenomenon under control. The motor using RE PMs, however, has higher efficiencies and no demagnetization problems, confirming the strong points of these magnets. Considering the material comparison, the benchmark motor also presents the lowest weight due to its smaller size. FeN magnets are confirmed to be by far environmentally convenient with much lower ELU and kgCO_2eq values than RE PMs, even though larger volumes of magnets are required. However, if the environmental impact of the whole motor is evaluated, the benchmark motor has the lowest environmental impact. Its small size saves iron and copper, and as a result, the reduced environmental impact of these materials compensates for that of PM RE.

It is fair to point out that the benchmark motor has a higher power density than the one designed with FeN with the highest current density value among all four designs. Such values will require different thermal management of the motors considered, which was not taken into account during this thesis work. In the case where such current density values are not achievable for thermal reasons, the motor would require to be longer to decrease the current while maintaining the

same torque. In that case therefore the amount of copper would be more similar, making the advantage of FeN magnets prevail.

To account for the different current values, the ELU value of the motor plus inverter system has been reported. Higher currents require larger inverters, which consequently have higher ELU values. Comparing these values, it can be seen that the SyR-e design has the lowest value despite being the design with the largest active length, highlighting how the current rating required also plays a key role in assessing environmental impact.

During this thesis work, no constraints on phase current were chosen because the focus was on demagnetization. Nevertheless, the choice of such a benchmark allows us to emphasize that although the environmental impact of RE-free magnets is far less, it must be considered that other materials also play a key role and consideration must be given to all of them when thinking about reducing environmental impact.

8.2 Future Developments

The use of RE-free magnets capable of replacing classical NdFeB magnets opens the way for further studies with the aim of improving their use for an increasingly sustainable future.

As could be seen from comparing the environmental impact of different designs, it is not only RE that represents a high environmental price to pay. The environmental footprint given by a material such as copper is something to consider if the overall environmental impact of a PMSM is to be reduced. An alternative might be to consider replacing copper windings with aluminum ones. In addition to the environmental benefit, the use of aluminum windings would also lead to a significant weight reduction because the density of copper is about three times that of aluminum. On the other hand, however, the efficiency of the motor would be affected because of the higher electrical resistivity of aluminum. It would therefore be a matter of evaluating the best compromise between these characteristics.

One aspect that could not be taken into account during this work is the ASC analysis. In designs that exploit RE PMs, it is important to evaluate the risk of demagnetization when an ASC is performed to protect the inverter from Uncontrolled Generator Operation (UGO). In the case of the use of Iron Nitride magnets,

we have seen how the normal operating current turns out to be the limit at which the phenomenon of demagnetization begins at the maximum torque points. It needs to be assessed the demagnetization behavior under ASC, although considering the typical values of short-circuit currents this would lead to an unacceptable demagnetization phenomenon for most points on the torque-speed map and this represents a real limit of putting in operation these motors.

During this thesis work, an attempt was made to understand if it was possible to use RE-free PMs instead of RE PMs and what this entailed. However, an interesting idea would be to evaluate the simultaneous use of RE and RE-free magnets. From the simulations carried out during this work, it was seen that the areas of the magnet that are most susceptible to the demagnetization phenomenon are always the same and are located near the outer edges (see Fig. 6.5). Therefore, the idea could be to reinforce the behavior against demagnetization by exploiting the segmentation of the magnets (typically used to reduce PM losses) by using RE magnets there where demagnetization would be greatest.

References

- [1] Shigeo Morimoto et al. “Experimental evaluation of a rare-earth-free PMASynRM with ferrite magnets for automotive applications”. In: *IEEE Transactions on Industrial Electronics* 61.10 (2014), pp. 5749–5756.
- [2] Han Xiong et al. “Permanet magnet demagnetization test fixture design and validation”. In: *2015 IEEE Energy Conversion Congress and Exposition (ECCE)*. IEEE. 2015, pp. 3914–3921.
- [3] Klaus J Schulz et al. *Critical mineral resources of the United States: economic and environmental geology and prospects for future supply*. Geological Survey, 2017, Chapter O.
- [4] Statista. *Distribution of rare earths production worldwide as of 2021, by country*. <https://www.statista.com/statistics/270277/mining-of-rare-earths-by-country/>. [Online; accessed 26-September-2022]. 2022.
- [5] Jost Wübbecke. “Rare earth elements in China: Policies and narratives of reinventing an industry”. In: *Resources Policy* 38.3 (2013), pp. 384–394.
- [6] Jun Cui et al. “Current progress and future challenges in rare-earth-free permanent magnets”. In: *Acta Materialia* 158 (2018), pp. 118–137.
- [7] European Commission. *Sustainable Recovery, Reprocessing and Reuse of Rare-Earth Magnets in a Circular Economy (SUSMAGPRO)*. <https://cordis.europa.eu/project/id/821114>. DOI 10.3030/821114. 2019.
- [8] Kenneth Henderson Jack. “The occurrence and the crystal structure of α -iron nitride; a new type of interstitial alloy formed during the tempering of nitrogen-martensite”. In: *Proceedings of the Royal Society of London. Series A. Mathematical and Physical Sciences* 208.1093 (1951), pp. 216–224.
- [9] TK Kim and Minoru Takahashi. “New magnetic material having ultrahigh magnetic moment”. In: *Applied Physics Letters* 20.12 (1972), pp. 492–494.
- [10] Yutaka Sugita et al. “Magnetic and Mössbauer studies of single-crystal Fe₁₆N₂ and Fe-N martensite films epitaxially grown by molecular beam epitaxy”. In: *Journal of Applied Physics* 76.10 (1994), pp. 6637–6641.

- [11] Jian-Ping Wang. “Environment-friendly bulk Fe16N2 permanent magnet: Review and prospective”. In: *Journal of Magnetism and Magnetic Materials* 497 (2020), p. 165962.
- [12] *SyR-e Software*. <https://sourceforge.net/projects/syr-e/>.
- [13] *FEMM Software*. <https://www.femm.info/wiki/Download>.
- [14] F. Cupertino S. Ferrari G. Pellegrino. *SyR-e User Manual*. 2022.
- [15] Gianmario Pellegrino, Simone Ferrari, and Gaetano Dilevrano. “Progettazione di Macchine a Magneti Permanenti Interni con SyR-e”. In: (2020).
- [16] Simone Ferrari and Gianmario Pellegrino. “FEAfix: FEA refinement of design equations for synchronous reluctance machines”. In: *IEEE Transactions on Industry Applications* 56.1 (2019), pp. 256–266.
- [17] Ahmed Selema, Mohamed N Ibrahim, and Peter Sergeant. “Mitigation of High-Frequency Eddy Current Losses in Hairpin Winding Machines”. In: *Machines* 10.5 (2022), p. 328.
- [18] Phil Mellor, Rafal Wrobel, and Nick Simpson. “AC losses in high frequency electrical machine windings formed from large section conductors”. In: *2014 IEEE Energy Conversion Congress and Exposition (ECCE)*. IEEE. 2014, pp. 5563–5570.
- [19] Alfredo Vagati et al. “Design of ferrite-assisted synchronous reluctance machines robust toward demagnetization”. In: *IEEE Transactions on Industry Applications* 50.3 (2013), pp. 1768–1779.
- [20] *JMAG Website*. <https://www.jmag-international.com/>.